Numerical analysis and design of concrete-filled wire arc additively manufactured steel tube under axial compression

Sha-Sha Song [a], Ju Chen [a], Guan Quan [a,*], Jun Ye [a,b,c,**], Yang Zhao [a]

[a] College of Civil Engineering and Architecture, Zhejiang University, Hangzhou, Zhejiang, China
[b] Center for Balance of Architecture, Zhejiang University, Hangzhou, Zhejiang, China
[c] School of Civil Engineering, University of Leeds, Woodhouse Lane, Leeds, LS2 9JT

ARTICLE INFO

ABSTRACT

Numerical investigation of the mechanical behaviour of concrete-filled wire arc additively manufactured (WAAM) steel tube under axial compression is presented in this paper. Typical structural performances of concrete-filled WAAM steel tube are extensively analyzed based on the experimental results firstly. FE models are established based on 3D models obtained by 3D laser scan technology, whilst the material anisotropy of WAAM steel tube is taken into account. The sensitivity study on the finite element (FE) model parameters is developed to assess their influence on the simulation results. The established FE models are verified against the test results demonstrating their effectiveness in predicting the structural behaviour of the concrete-filled WAAM steel tube. The composite action between the WAAM steel tube and inner concrete is analyzed through the validated FE models, indicating that it should be emphasized within the strain range from 0.003 to 0.01. The influences of the concrete and steel strengths are evaluated to investigate the confinement effect, showing that the concrete and steel strength exhibit a negative and positive impact on the confinement effect, respectively, and a positive correlation between the steel strength and biaxial stresses of the WAAM steel tube can be obtained. Finally, the design method of concrete-filled WAAM steel tube under axial compression, which considers the effect of the geometric undulations and material anisotropy of the WAAM steel tube, is proposed based on the theory of confining effect. The comparison results indicate that the proposed method can predict the axial compressive strengths of the concrete-filled WAAM steel tubes with reasonable accuracy.

1. Introduction

Among the various metal directed energy deposition (DED) technologies, the present study focuses on the wire arc additive manufacturing (WAAM) process [1–6], as illustrated in Fig. 1. WAAM has the potential for a significant impact on the construction industry due to its ability to produce large parts compared with powder bed fusion (PBF) technology. For example, the world's first large-scale construction of WAAM structural elements, i.e. the 3D-printed steel foot bridge - see Fig. 2, was 3D printed by the Dutch start-up company MX3D (www.mx3d.com) [7]. The structural behaviour of the bridge is clearly beyond the scope of current steel structure design specifications [8–11]. The novel structure, therefore, has required extensive experimental and numerical research for its safety to be demonstrated. Laghi et al. [4] and Gardner et al. [5] have conducted experimental tests for

the characterization of small specimens taken from planar sheets and full-scaled tubes manufactured by MX3D using the WAAM process. Advanced finite element (FE) modelling of the bridge and its components has also been performed and presented [12].

Generally, the development in construction industry of WAAM technology depends on a good standing on the structural behaviour and the development of design guidelines for metal 3D printed components and structures. Therefore, the mechanical behaviour and design of 3D printed elements manufactured by PBF have been investigated [13–16]. Due to the potential application in large-scale structures, the research of WAAM structures is mainly on experimental tests of material properties [13], bolted [14,15] and T-stub [16] connections, square hollow sections (SHS) and circular hollow sections (CHS) components [4,5,12, 17–20], whilst the study on the mechanical behaviour of concrete-filled WAAM steel is still rare.

Concrete-filled steel tube (CFST) is one of the most widely used

Nomenclature

Latin upper case letters

A	the average cross-section area of the WAAM steel tube
A_c	the cross-sectional area of inner concrete
A_s	the cross-sectional area of WAAM steel tube
A_{min}	the minimum cross-section area of the WAAM steel tube
A_{max}	the maximum cross-section area of the WAAM steel tube
D	the average outer diameter of the WAAM steel tube
D_{max}	the maximum outer diameter of the WAAM steel tube
D_{min}	the minimum outer diameter of the WAAM steel tube
D_c	the diameter of inner concrete
D_{CDM}	the damage factor introduced based on the continuum damage mechanics (CDM)
DI	the ductility index of the CFST specimen
E	the energy dissipation of the whole CFST specimen
E_c	the elastic modulus of concrete being used
E_s	the elastic modulus of WAAM steel being used
$(EA)_{sc,Exp}$	the axial stiffness of the CFST specimen obtained by test results
G_F	the fracture energy of steel
K_0	the elastic stiffness of the cross-section in the original state without damage
K^*	the secant stiffness of cross-section damage
L_o	the length of the tested CFST specimens
N_u	the compressive strength of the concrete-filled WAAM steel tube
$N_{u,AISC}$	the predicted compressive strength of the concrete-filled WAAM steel tube using AISC 360–16
$N_{u,ACI}$	the predicted compressive strength of the concrete-filled WAAM steel tube using ACI 318
$N_{u,AIJ}$	the predicted compressive strength of the concrete-filled WAAM steel tube using AIJ
$N_{u,AS}$	the predicted compressive strength of the concrete-filled WAAM steel tube using AS 5100
$N_{u,EC4}$	the predicted compressive strength of the concrete-filled WAAM steel tube using EC4
$N_{u,Exp}$	the experimental compressive strength of the CFST specimens
$N_{u,FE}$	the numerical compressive strength of the concrete-filled WAAM steel tube
$N_{u,GB}$	the predicted compressive strength of the concrete-filled WAAM steel tube using GB 50936
$N_{u,Design}$	the predicted compressive strength obtained from the proposed design method
$N(\Delta)$	the axial load of the CFST specimen during the loading stage
R_{ij}	the anisotropic yield stress ratios
SI	the strength index of the CFST specimens
T	the average thickness of the WAAM steel tube
T_{max}	the maximum thickness of the WAAM steel tube
T_{min}	the minimum thickness of the WAAM steel tube
V	the volume of the whole CFST specimen

Latin lower case letters

f_1	the lateral confining pressure of concrete
f_c	the cylinder compressive strength of concrete being used
f_{ck}	the characteristic strength of concrete
f_{cu}	the cubic compressive strength of concrete being used
f_y	the yield strength of WAAM steel being used
$f_{y,s}$	the yield strength of WAAM steel tube
f_{y,s_90}	the yield strength of the WAAM steel tube with a deposition direction of 90°
f_{y,s_0}	the yield strength of the WAAM steel tube with a deposition direction of 0°
f_t	the tensile fracture stress of concrete being used
f_u	the ultimate strength of WAAM steel being used
$f(\sigma)$	Hill's potential function
$u_{0.75}$	the axial displacement of specimen when the load attains 75% of the axial compressive strength in the pre-ultimate stage
$u_{0.85}$	the axial displacement of specimen when the load falls to 85% of the axial compressive strength
u_p	the axial displacement of specimen when attainment of the axial compressive strength
w	the energy dissipation density of the CFST specimen

Greek case letters

α	the ratio of the circumferential stress of the WAAM steel tube to the yield stress f_{y,s_90}
α_{sc}	the confinement factor of the CFST members
β	the ratio of the longitudinal stress of the WAAM steel tube to the yield stress f_{y,s_90}
σ_c	the longitudinal stress of the inner concrete
σ_{con}	the confinement stress of the inner concrete provided by the steel tube
σ_{ij}	the stress component of steel element
$\sigma_{s,L}$	the longitudinal stress of the WAAM steel tube
$\sigma_{s,\theta}$	the circumferential stress of the WAAM steel tube
σ^0	f_{y,s_0} the reference yield stress specified for the metal plasticity definition
$\varepsilon_{0.75}$	the axial strain of the specimen when the load attains of 75% the ultimate load in the pre-ultimate stage
$\varepsilon_{0.85}$	the axial strain of the specimen when the load falls to 85% of the ultimate load
ε_b	$\frac{\varepsilon_{0.75}}{0.75}$
$\varepsilon_{c,c}$	the axial strain of confined concrete at f_c
ε_f	the fracture strain of WAAM steel being used
ε_{sh}	the hardening strain of steel
ε_u	the ultimate strain of steel
ε_y	the yield strain of steel
τ	bond stress critical value of steel tube and concrete interface
τ^0	the reference yield stress specified for the metal plasticity definition
ν_{sc}	the ratio of the circumferential strain to longitudinal strain
Δ	the axial displacement of the CFST specimen during the loading stage

composite components in CFST structures [21–29], such as CFST arch bridges and CFST transmission towers. The steel tube and inner concrete are capable of supporting each other meanwhile working together to produce composite structural members with confinement effects between steel and concrete. For circular CFST subjected to the axial compressive load, their compressive strength can be improved due to the lateral confinement effect provided by the circular steel tube to the inner concrete. Most of the current research is limited to the circular CFST

with conventional steel elements, in terms of experimental and numerical studies [30–36]. The geometric characteristics of WAAM steel tubes are more variable than those of rolled sections due to the surface undulations arising from the printing process, rendering that the bond strength between the WAAM steel tube and concrete can be significantly enhanced [37]. Unlike CFST members fabricated from conventional steel tubes (the seam welds running along the length of fabricated tubes) where fracture of the steel tubes is often observed [38,39], the WAAM
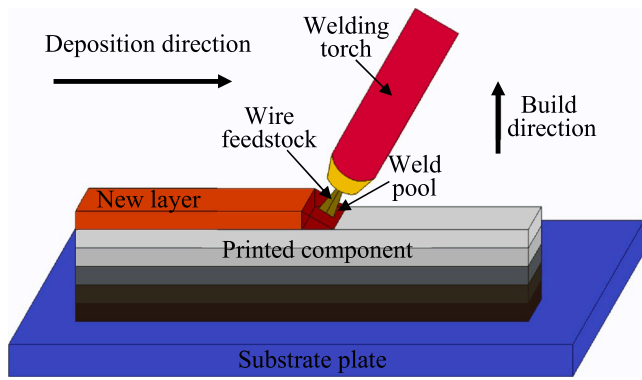
Fig. 1. Schematic diagram of the WAAM process.

tubes are composed of continuously printed 'hoop' and the resulting in good deformation capacity, with a positive impact on the ductility of the CFST with WAAM element after the attainment of ultimate capacities [40]. The structural behaviour of concrete-filled WAAM steel tubes has been rarely studied. When it comes to circular CFST elements, the research has been limited to the investigation of the compressive and interfacial bond behaviour of circular concrete-filled WAAM steel tubes experimentally [37,40]. Seeking to fill this gap, the mechanical behaviour of circular concrete-filled WAAM steel tube under axial compression is investigated numerically in this paper.

The extensive experimental research and numerical investigation of concrete-filled WAAM steel tubes are presented. Typical performance measurements of concrete-filled WAAM steel tube, namely stiffness, ductility, energy dissipation, damage and strain ratio, are extensively analyzed based on the experimental results. The FE models are established from the 3D models obtained by the 3D laser scanning, and the material anisotropy of WAAM steel is taken into account. The sensitivity study of the FE models is conducted to investigate the influence of element type, element size, structural grid members and friction factor on the FE model analysis. The established FE models are verified against the existing test results. The composite action between the WAAM steel tube and inner concrete is analyzed through the validated FE models. The influences of the concrete strength and steel strength on element stresses and axial compressive strength index of concrete-filled WAAM steel tube are evaluated to study the confinement effect provided by the steel tube to concrete. Finally, the design formulations of concrete-filled WAAM steel tubes under axial compression, which consider the influence of geometric undulations and material anisotropy, are proposed based on the theory of confining effect.

2. Summary of experimental investigations

2.1. Test program

2.1.1. Specimens with WAAM technology

The production process of CFST specimens with WAAM technology is illustrated in Fig. 3. Firstly, nine CHS steel tubes were printed with WAAM technology based on the nominal diameter-to-thickness ratios in the range 30–100 and nominal length to diameter ratios in the range 3.3–6.7. The applied welding torch of WAAM technology consisted of a six-axis robot arm and a metal inert gas (MIG) welding machine. The welding torch printed the component layer-upon-layer according to the printing paths which were obtained from the computer-aided design models. The wire feedstock supplied to the welding torch was heated, melted and deposited onto a substrate plate of steel grade Q235B, as shown in Fig. 1. Then the components were built up layer by layer. The feedstock material was ER50–6 mild steel wire which is a widely used solid wire for gas shielded welding. The tensile and yield strengths of ER50–6 wire are larger than 500 MPa and 420 MPa, respectively. The shield gas in the deposition process was a mixture of 97% Ar and 3% CO_2.

3D laser scans were employed subsequently to obtain the geometry of the printed steel tubes digitally. The digital models were then used to acquire an accurate and detailed surface morphology which can be imported to the ABAQUS [41] software for numerical analysis of the CFST specimens, as shown in Fig. 3. After that, the concrete was filled into the WAAM steel tube, allowing to cure for 24 days. Then, the upper end plate of each WAAM steel tube was welded. After that the surfaces of the WAAM steel tubes were treated and strain gauges were attached to these tubes – see Fig. 3 (process 4). Therefore, the first CFST specimen and concrete cube were tested soon after the completion of the 28 days curing period. A 20 mm thick end plate was welded to each end of the specimens to facilitate the application of the compressive load during testing and to ensure load even distribution. Summary of the geometric dimensions of the specimens which were obtained from the scanned digital models [40], are reported in Table 1, where T, T_{min} and T_{max} are the average, minimum and maximum thicknesses of the WAAM steel tube, respectively; D, D_{min} and D_{max} are the average, minimum and maximum outer diameters of the WAAM steel tube, respectively; A, A_{min} and A_{max} are the average, minimum and maximum values of the cross-sectional areas of the WAAM steel tube, respectively. The specimens are varied through appropriate labelling, which includes the nominal outer diameter, thickness and length of the WAAM steel tube. To illustrate, the label "D180T3L600" signifies a specimen with a nominal outer diameter of 180 mm, a nominal thickness of 3 mm and a nominal length of 600 mm.

The monotonic tensile tests were conducted to obtain the material properties of WAAM steel. Tensile coupons were cut from WAAM sheet material at 0° and 90° to the deposition direction, as shown in Fig. 4, to
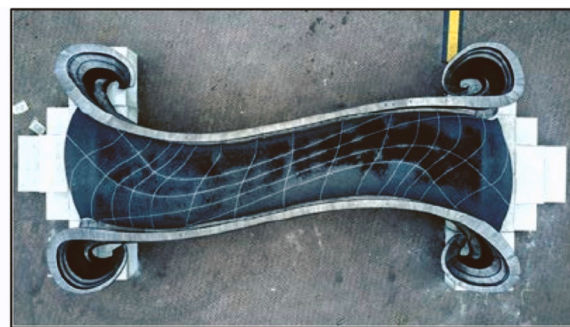
Fig. 2. MX3D (www.mx3d.com) bridge was presented at the Dutch Design Week 2018 in Eindhoven [12].
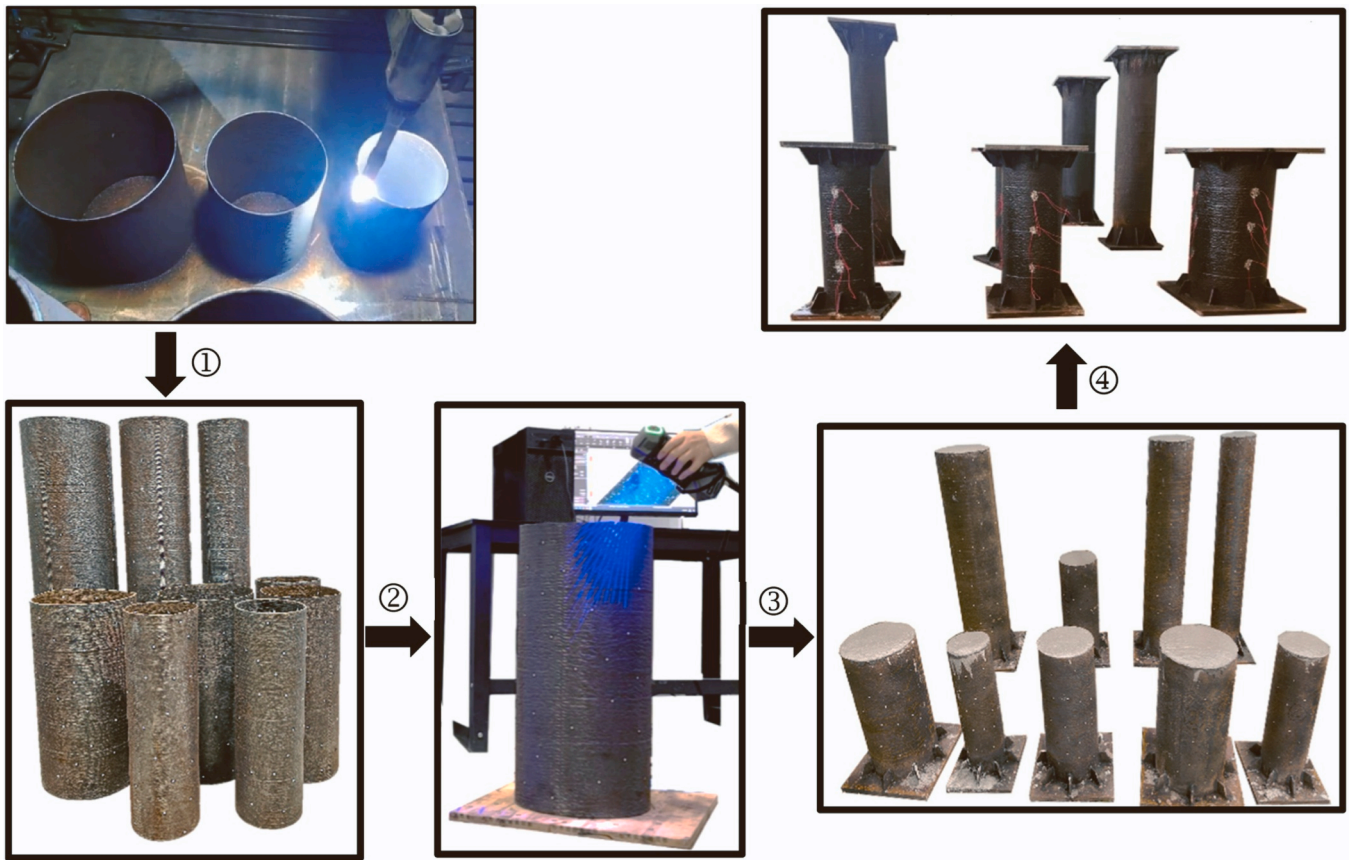
Fig. 3. The production process of CFST specimens with WAAM technology.

Table 1
Summary of the real geometric dimensions of the CFST specimens as determined by the laser scans.

CFST specimens	T (mm)	T_{min} (mm)	T_{max} (mm)	D (mm)	D_{min} (mm)	D_{max} (mm)	A (mm^2)	A_{min} (mm^2)	A_{max} (mm^2)
D180T3L600	2.89	2.67	3.16	178.08	177.73	178.34	1591.16	1468.90	1739.27
D240T3L600	3.00	2.83	3.28	237.94	237.81	238.11	2214.03	2090.87	2417.61
D300T3L600	3.06	2.98	3.26	295.23	295.08	295.46	2844.25	2735.34	2989.63
D180T6L600	6.44	6.11	6.73	178.46	178.49	178.89	3478.71	3309.13	3638.19
D240T6L600	6.40	6.16	6.78	238.19	238.35	238.77	4661.17	4494.62	4939.92
D300T6L600	6.47	6.15	6.94	297.90	298.25	298.09	5928.27	5643.85	6344.65
D180T4L1200	3.53	3.15	3.87	178.91	178.69	179.23	1944.79	1734.64	2129.98
D240T4L1200	3.70	3.17	4.04	239.00	238.63	239.25	2732.96	2342.80	2986.09
D300T4L1200	3.66	3.18	3.99	298.57	298.46	298.89	3391.51	2953.88	3692.44

consider the WAAM material anisotropy. A summary of the average material properties in 0° and 90° to the deposition directions for the WAAM steel coupons are reported in Table 2, in which E_s is the elastic modulus of WAAM steel; f_y and f_u are the yield and ultimate strengths, respectively; ε_f represents the fracture strain. The material properties of the filled concrete were determined by conducting compressive tests on four concrete cubes. These tests allowed for the calculation of the mean compressive strength of the concrete cubes. $f_{cu} = 41.33$MPa is the cubic compressive strength of concrete.

2.1.2. Axial compressive test

The experimental setup is shown in Fig. 5(a). Electric-hydraulic compression equipment with a capacity of 10,000 kN was used for applying the axial load [42,43], with a loading rate of 1 mm/min. To guarantee a proper transfer of actions between the end plates of the specimens and the loading plates, spherical hinge supports were employed.

For CFST specimens shorter than 1000 mm in length, eight LVDTs

(D1-D8) were installed symmetrically at both the top and bottom ends to measure the vertical displacement. In the case of specimens longer than 1000 mm, two additional LVDTs (D9 and D10) were included to measure the lateral displacement, as illustrated in Fig. 5(a). To measure both vertical and horizontal strains, a total of twelve transverse strain gauges ($S_{T1} \sim S_{T12}$) and twelve sixteen longitudinal strain gauges ($S_{L1} \sim S_{L12}$) were installed on the specimens as shown in Fig. 5(b). Throughout the test, data from the loading cells, LVDTs and strain gauges were gathered using a DH3817 static data acquisition system at a frequency of 1 Hz [43, 44].

2.2. Test results

2.2.1. General structural behaviour

The load-end shortening curves resulting from the axial compression tests of all CFST specimens are presented in Fig. 6. In the early loading phase, the curves show a linear relationship between load and end shortening and small deformations can be observed on the WAAM steel
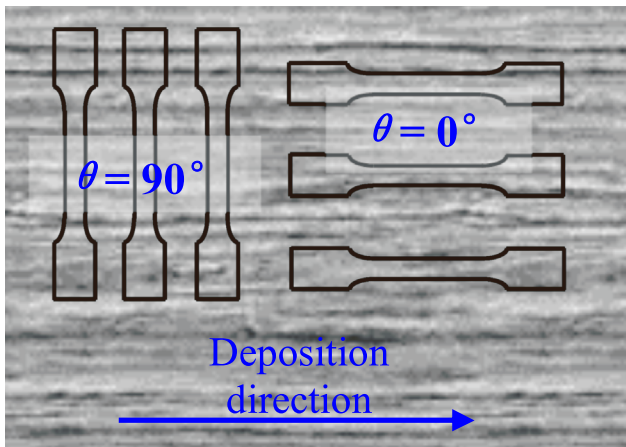
Fig. 4. Orientation of tensile coupons extracted from WAAM plate relative to deposition direction.

Table 2
Material properties of the WAAM steel coupons.

θ	t_n (mm)	E_s (GPa)	f_y (MPa)	f_u (MPa)	ε_f	Note
90°	6	205	405	513	0.20	As-built
		199	420	535	0.17	Machined
	3	198	408	515	0.09	As-built
0°	6	209	411	522	0.24	As-built
		199	445	551	0.18	Machined
	3	186	478	563	0.15	As-built

surface, indicating that the specimens were in the elastic stage. As the load continued to increase, the specimens transitioned into the elastic-plastic stage. In this stage, the WAAM tube started to yield with substantial deformation, and the stiffness of each specimen gradually decreased. Eventually, the inner concrete was crushed, and the WAAM tube showed pronounced local buckling deformation, resulting in the specimens attaining their axial compressive strength [40].

Fig. 7 presents the failure modes of the specimens. From the deformation of the outer surface of the steel tube, it can be found that the concrete crushing failure modes included outward folding and shear

deformation [40]. Table 3 provides a summary of the axial compressive strength $N_{u,Exp}$ of the specimens in the experiments. To evaluate the composition action of inner concrete and steel tube, a strength index *SI* is defined as follows:

$$SI = \frac{N_{u,Exp}}{f_{y,s}A_s + f_c A_c} \qquad (1)$$

where $f_{y,s}$ is the average yield strength of the WAAM steel tube; $f_c = 0.8f_{cu}$ is the cylinder compressive strength; A_s and A_c are the cross-sectional area of the WAAM steel tube and inner concrete, respectively. The strength index *SI*, therefore, is determined and listed in Table 3. It can be seen that the values of strength indexes for all specimens are stable at around 1.2, indicating that the interaction of tube and concrete shall be considered in the axial compressive strength of the concrete-filled WAAM steel tube. Thus the confinement factor shall be further analyzed when proposing a new strength design method for the concrete-filled WAAM steel tube under axial compression.

2.2.2. Typical mechanical behaviour
(1) Stiffness.

Generally, the load axial strain curves exhibited clear elastic-plastic behaviour when the load reached approximately 60–75% of the ultimate bearing capacity $N_{u,Exp}$, as shown in Fig. 6. The slope of the line extending from the origin to 40% of $N_{u,Exp}$ was considered to determine the axial stiffness $(EA)_{sc,Exp}$ of the CFST specimens [45]. Table 3 provides a summary of the stiffness values from the test results, while Fig. 8(a) shows both the experimental and calculated results of stiffness for all specimens. It can be seen that the experimental stiffnesses for all specimens are always somewhat larger than the corresponding calculated values except for D180T6L600 and D240T6L600, indicating that the composite stiffness of the specimen is larger than a simple summation of the stiffness of concrete and tube. For D180T6L600 and D240T6L600 specimens, their experimental stiffnesses are somewhat lower than the corresponding calculated values, this is because the calculated values are overestimated based on the average cross-sectional area (A_s) for the WAAM steel tube due to less uniform cross-sectional areas of the thicker WAAM steel tube.

(2) Ductility.

To investigate the ductility of the CFST specimens, a ductility index *DI* [31,45–48] was adopted in this paper. The corresponding ductility index is defined as follows:

(a) Test setup   (b) Arrangement of strain gauges
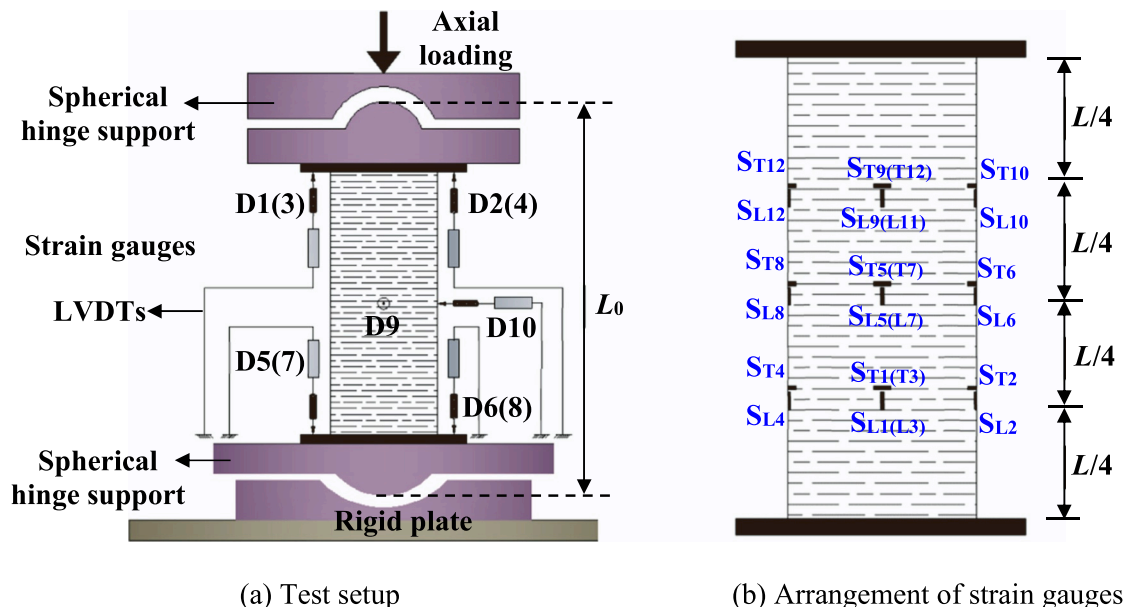
Fig. 5. Setup and measurements of axial compressive test for the CFST specimens.

(a) D180 series

(b) D240 series

(c) D300 series
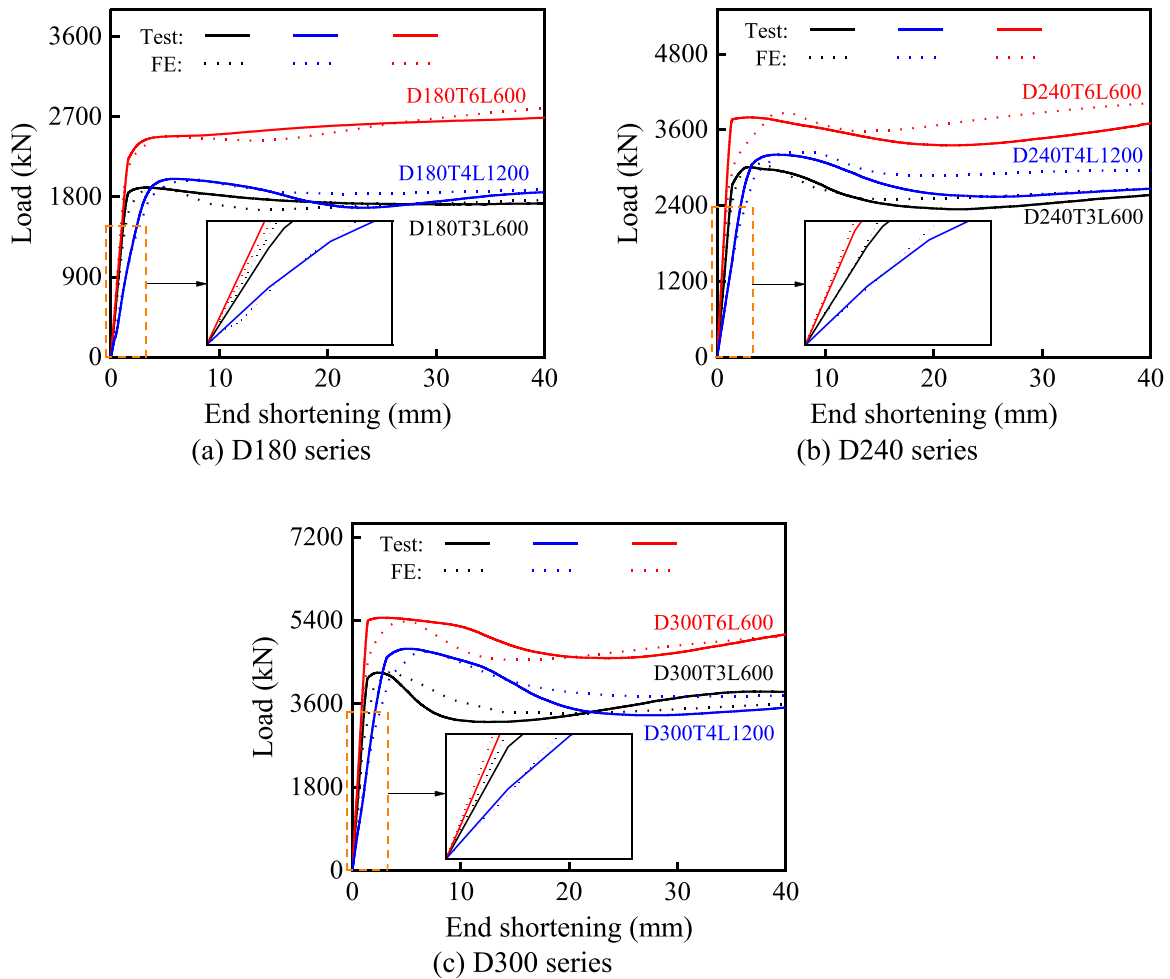
Fig. 6. Comparison of load-end shortening curves between test and FE results.

$$DI = \frac{\varepsilon_{0.85}}{\varepsilon_{b}} \qquad (2)$$

where $\varepsilon_{0.85}$ is the axial strain of specimen when the load falls to 85% of the axial compressive strength; ε_{b} is equal to $\varepsilon_{0.75}/0.75$, and $\varepsilon_{0.75}$ is the axial strain of specimen when the load attains 75% of the axial compressive strength in the pre-ultimate stage. It should be noted that for the specimens without a 15% decrease in ultimate load after attainment of the axial compressive strength, the strain of the limit point $\varepsilon_{0.85}$ can be calculated by three times the displacements at their ultimate load [46–48].

The ductility indexes *DI* calculated by Eq. (2) for all specimens are shown in Table 3 and are plotted in Fig. 8(b) against the tube diameter to wall thickness ratio *D/T* and compared with the ductility index of the CFST members comprising conventional steel tubes [30,31,49–51]. The results show that the range of calculated *DI* for the CFST specimen varied from 4.50 to 7.06. For the conventional CFSTs with concrete grades of C40-C50 [30,49,50], the ductility indexes of the CFST specimens and conventional CFSTs are basically the same, with values around 6. For the conventional CFSTs with a concrete grade of C30 [51], the ductility indexes of the CFST specimens are less than that of the conventional CFSTs. For the conventional CFSTs with a concrete grade of C80 [31], the ductility indexes of the CFST specimens are greater than that of the conventional CFSTs. It is attributed to the poor ductility of high-strength concrete. It should be mentioned that the WAAM tubes being composed of continuously printed 'hoops' with high ductility, it is able to effectively resist the outward pressure from the confined concrete, in contrast to the seam welds running along the length of conventionally fabricated

tubes. Future research, therefore, needs to focus on comparing the ductility of the WAAM steel tubes with conventional steel tubes.

(3) Energy dissipation.

Energy dissipation density (*w*) is an important indicator reflecting the ability of a CFST member to absorb energy from the origin to the ductility being fully utilized [46]. Energy dissipation density can be defined as follows:

$$w = \frac{E}{V} \qquad (3)$$

where $E = \int_{0}^{\Delta} N(\Delta)d\Delta$ is the value of energy dissipation of the whole CFST specimen, as illustrated in Fig. 9(a); $N(\Delta)$ is the axial load of the specimen; Δ is the axial displacement of the specimen; *V* is the volume of the whole specimen. To ensure that all specimens can fully utilize their ductility, the energy dissipation value corresponding to the 20 mm axial displacement of each specimen is taken to calculate the energy dissipation density based on the ductility definition in the previous summary, as shown in Fig. 9(b).

Calculated energy dissipation densities are summarized in Table 3. It can be seen that the energy dissipation density of the specimen decreases with an increase in the specimen height and increases with an increase in the steel ratio. The results demonstrate the stub specimen exhibits a stronger ability to absorb energy than the long specimen, and the increase in steel ratio can improve the energy absorption capacity of concrete-filled WAAM steel tube, resulting in a better structural behaviour of the CFST members.

(4) Damage.

(a) D180T6L600

(b) D240T6L600

(c) D300T6L600

(d) D180T4L1200

(e) D300T4L1200

Fig. 7. Comparison of failure mode between test and FE results.

Table 3
Summary of the test results for the CFST specimens.

CFST specimens	$N_{u,Exp}$(kN)	SI	$(EA)_{sc,Exp}\times10^6$	DI	W (kJ/m³)
D180T3L600	1904	1.29	0.96	6.25	2278
D240T3L600	3010	1.27	1.67	7.06	1898
D300T3L600	4274	1.25	2.56	4.50	1613
D180T6L600	2428	1.16	1.17	5.39	3118
D240T6L600	3797	1.21	1.92	6.75	2568
D300T6L600	5460	1.24	2.96	5.79	2333
D180T4L1200	2002	1.23	1.12	5.23	1141
D240T4L1200	3208	1.23	1.80	5.39	1004
D300T4L1200	4791	1.29	2.66	4.93	948

The damage evolves along with concrete crushing and steel yielding as the deformation increases of CFST members. To quantitatively describe the damage evolution process and damage degree of the CFST specimen, the damage factor D_{CDM} was introduced based on the continuum damage mechanics (CDM):

$$D_{CDM} = 1 - \frac{K^*}{K_0} \tag{4}$$

where K_0 is the elastic stiffness of the cross-section in the original state without damage; K^* is the secant stiffness of cross-section damage, which takes the secant slope of the N-Δ curve.

Fig. 8(c) shows the damage evolution process against the deformation of the CFST specimen. At the initial stage of loading, the curve shows as a platform segment with a D_{CDM} value close to 0. This indicates that the specimens are in the elastic stage without damage. When the axial displacements reach 0.8–2.0 mm, damage to the specimens begins to develop, resulting in cracks developing in the inner concrete and yielding in the steel tube. The significant growth of D_{CDM}, subsequently, can be found in the curves, as illustrated in Fig. 8(c), which indicates that damage rapidly develops in these specimens at the elastic-plastic stage. After that, the cross-sectional strength of the WAAM steel tube reaches the yielding platform, resulting in the confinement effect of the concrete being relatively stable and the damage development rate tends to flatten out until the specimen fails. In addition, it can also be observed that the damage development rate is relatively consistent for specimens of the same height.

(5) Strain ratio.

Fig. 8(d) shows the relationship of the normalized axial load (N/N_u) against the strain ratio (ν_{sc}) of all specimens. The strain ratio is defined as the absolute value of the circumferential strain divided by the longitudinal strain of the steel tube at each gauged point and represents the composite action between the steel tube and the inner concrete. With larger the strain ratio is, there will be more significant composite actions between the steel tube and the inner concrete [52].

It can be observed from Fig. 8(d) that at the initial loading stage, the strain ratio is close to Poisson's ratio of steel (about 0.25–0.3) and it increases slowly until the load reach 10% of the axial compressive strength. Although the stress ratio of the steel tube has increased at this stage, the inner concrete is still hardly enhanced by the steel tube

(a) Stiffness

(b) Ductility

(c) Damage evolution process

(d) Strain ratio
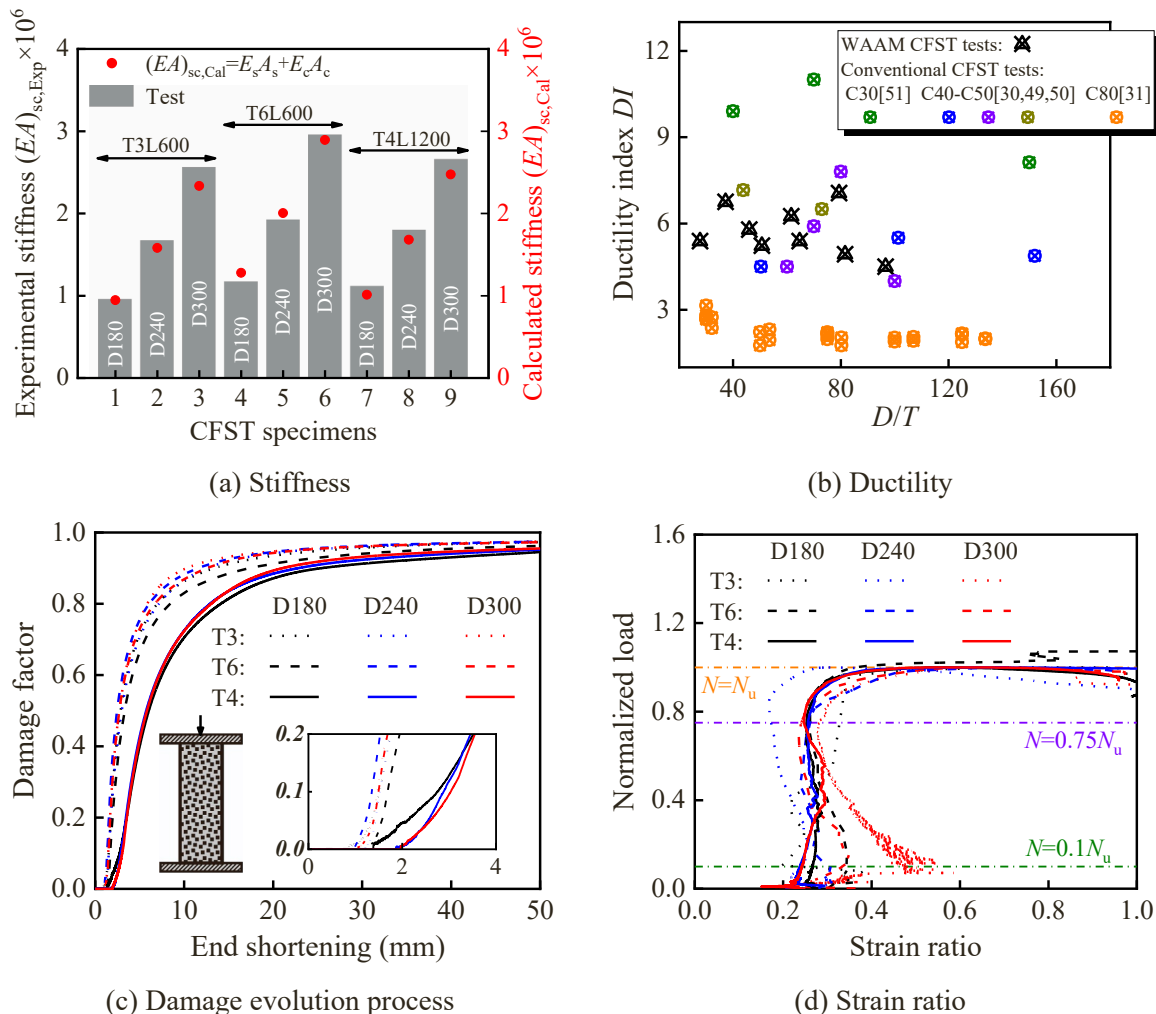
Fig. 8. Comparison of typical mechanical behaviours.

(a) Region of energy dissipation

(b) Displacement of energy dissipation
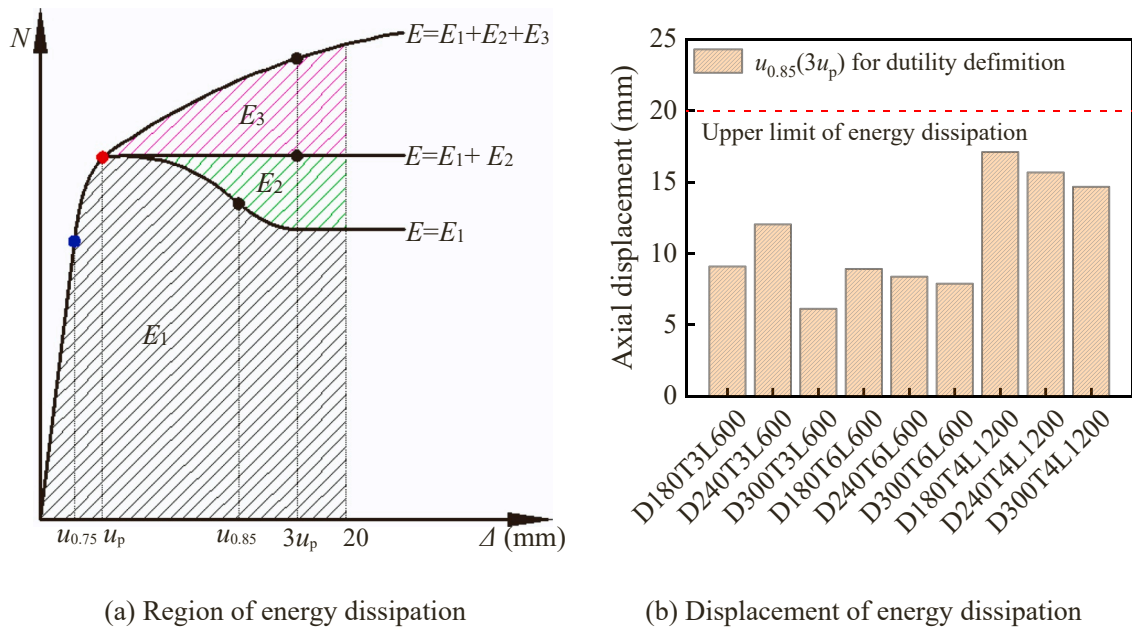
Fig. 9. Diagram of energy dissipation calculation.
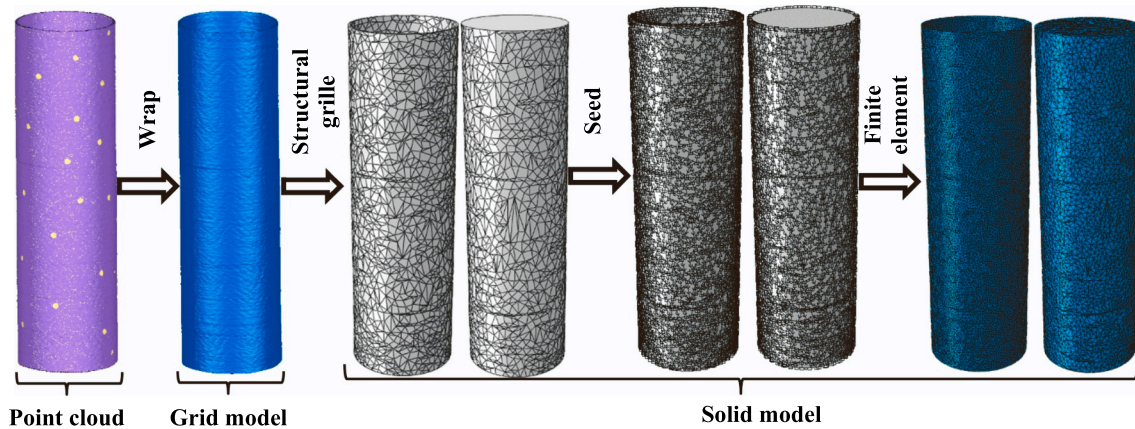
Fig. 10. Reverse reconstruction model process based on 3D scanning point cloud.

because Poisson's ratio of the inner concrete is lower than that of the steel tube during this stage. After that, the strain ratio decreases as the load increases to $0.75N_u$ at the elastic stage. It proves again that no confinement exists during the initial loading stage, otherwise, the stress ratio should continue to increase at the elastic stage. In addition, the decrease in strain ratio may be due to the anisotropy of the WAAM steel. After the load is greater than $0.75N_u$, the strain ratio increases significantly with an increase in load. During this stage, the confinement effect provided by steel tube to inner concrete increases as the strain ratio increases. All specimens reach their compressive strength when the strain ratio is about 0.4–0.6, and then the increase in strain ratio (confinement effect) does not improve the axial compressive strength of the specimens due to the concrete crushing and steel yielding in this stage.

3. Finite element modelling and validation

The FE modelling was developed after the testing programme to obtain an insight into the confinement effect between the steel tube and inner concrete. The developed numerical model enabled further insight into the more detailed structural response and was also used for parameter analysis. The FE models were developed using ABAQUS [41].

3.1. Finite element modelling methodology and analysis

3.1.1. Structural model reconstruction

The process of reverse reconstruction model based on the 3D scanning model is illustrated in Fig. 10. After the overall surface of the printed steel tube was scanned completely, the 3D point cloud of the whole specimen was obtained in a file of "asc" format. The output point cloud file, subsequently, was wrapped to form a closed grid model in a file of "stl" format, allowing the point data to be de-noised and optimized and the holes in the surface of the steel tube were patched to form a closed 3D surface model. The grid model, therefore, be further input into the Rhinoceros [53], in which the polygon count was reduced to ensure both actuarial accuracy (retaining the key geometrical features of the steel tube) and computational efficiency. The grid model was converted into the solid model in a file of "step" format. Finally, a 3D solid model of the steel tube in "step" format was input to the FE software ABAQUS [41] and the corresponding 3D solid model of inner concrete was established using the surface morphology of the steel tube based on Boolean operation.

3.1.2. Boundary conditions, elements, and constraints

The details of the developed FE model of the CFST specimen are

$d_2=d_3=0$, d_1=applied load, $r_2=r_3=0$ coupled with all displacements and rotations of the column end based on global coordinates

RP-1

Tube, C3D10

Concrete, C3D10

RP-2

$d_1=d_2=d_3=0$, $r_2=r_3=0$ coupled with all displacements and rotations of the column end based on global coordinates

Concrete surface

Tube surface
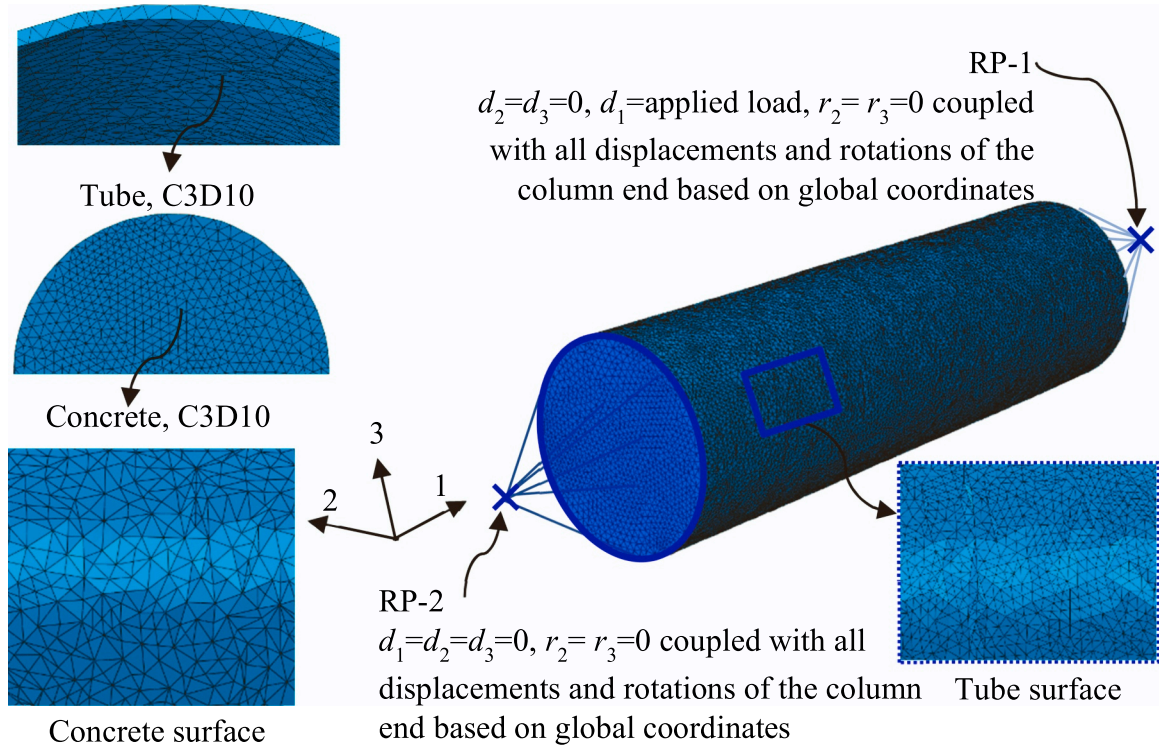
Fig. 11. Schematic view of the FE model.

shown in Fig. 11. The boundary conditions were applied as the test set-up where all degrees of freedom at both CFST column ends were coupled to the Reference Points 1–2 (RPs 1–2), respectively. RP 2 was at the bottom end of the column, and all degrees of freedom were constrained except "r_1". RP 1 was at the top end of the column, and all degrees of freedom were constrained except "d_1" and "r_1". The axial load was applied to the RP 1 by displacement control and the loading speed was consistent with the test.

The CFST specimen coupled with its high geometric complexity presented challenges in defining the FE mesh. Thus a sensitivity study shall be developed to assess the influence of element type, element size, structural grid members and friction factor on the FE results. Due to the random distribution of structural grids on the surface of the solid model, as shown in Fig. 10, the FE model adopts free mesh division technology for seeding and meshing. Two element types can be selected for the mesh division technology [41], i.e. four-node linear tetrahedron solid element (C3D4) and ten-node quadratic tetrahedron solid elements (C3D10). In addition, the different element sizes (5 mm, 8 mm and 10 mm for steel; 10 mm, 15 mm and 20 mm for concrete) were also analyzed in the mesh sensitivity study. For the concrete-tube interface, different friction coefficients, from 0.2 to 0.8, in the tangential direction were assumed for the Coulomb friction model and the hard contact behaviour in the normal direction was employed. The bond stress critical value τ limit between the steel tube and inner concrete can be calculated by $\tau = 2.314 - 0.0195(D_c/T)$, in which D_c is the diameter of inner concrete; T is the thickness of steel tube.

The sensitivity study results of FE model parameters are shown in Fig. 12. To compare the computational efficiency of each model, a CPU speed of 48 cores per hour was used to analyze each FE model. It can be found that using various parameters had little effect on the load-displacement curves but the models with more element and structural grid members would cost longer calculation time. Although the C3D4 element can ensure higher computational efficiency, it may lead to instability in model calculations. From the sensitivity study, C3D10 elements with 10 mm and 20 mm size for steel and concrete, respectively, were adopted as well as 5000 structural grid for scanned steel tubes and

a friction coefficient of 0.6 in the Coulomb friction model was employed, providing a balance between an accurate representation of the key geometrical features, computational efficiency and obtained satisfactory results.

3.1.3. Material

The anisotropic yield model was used for the printed steel that exhibits different yield behaviour in different directions, which was introduced through defined stress ratios R_{ij} that were applied in Hill's potential function. Hill's potential function is a simple extension of the Mises function, which can be expressed in terms of rectangular Cartesian stress components as:

$$f(\sigma) = \sqrt{F(\sigma_{22} - \sigma_{33})^2 + G(\sigma_{33} - \sigma_{11})^2 + H(\sigma_{11} - \sigma_{22})^2 + 2L\sigma_{23}^2 + 2M\sigma_{31}^2 + 2N\sigma_{12}^2}$$

(5)

where F, G, H, L, M and N are constants obtained by tests of the material in different orientations. They are defined as:

$$F = \frac{1}{2}\left(\frac{1}{R_{22}^2} + \frac{1}{R_{33}^2} - \frac{1}{R_{11}^2}\right)$$

(6)

$$G = \frac{1}{2}\left(\frac{1}{R_{33}^2} + \frac{1}{R_{11}^2} - \frac{1}{R_{22}^2}\right)$$

(7)

$$H = \frac{1}{2}\left(\frac{1}{R_{11}^2} + \frac{1}{R_{22}^2} - \frac{1}{R_{33}^2}\right)$$

(8)

$$L = \frac{3}{2R_{23}^2}$$

(9)

$$M = \frac{3}{2R_{13}^2}$$

(10)

$$N = \frac{3}{2R_{12}^2}$$

(11)

(a) Friction factor

(b) Element size

(c) Structural grid members
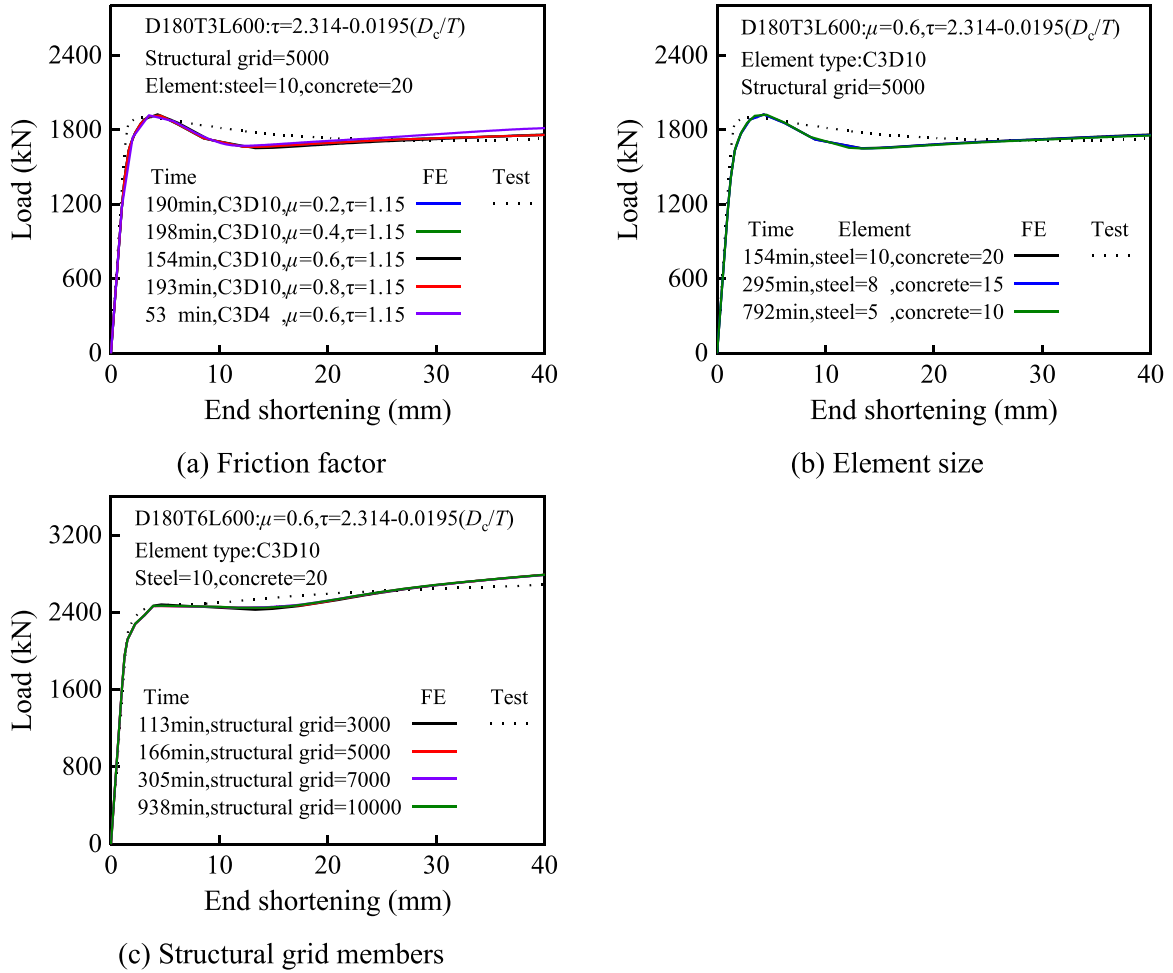
Fig. 12. Sensitive study of FE model parameters.

$$\sigma_{ij} = \begin{cases} R_{ij}\sigma^0 & (i = j) \\ R_{ij}\tau^0 = \dfrac{R_{ij}\sigma^0}{\sqrt{3}} & (i \neq j) \end{cases} \tag{12}$$

where σ_{ij} is applied as the only nonzero stress component; τ^0 and σ^0 is the reference yield stress specified for the metal plasticity definition; R_{ij} are anisotropic yield stress ratios. Anisotropic yield behaviour was modelled through the use of yield stress ratios R_{ij}, as expressed in Eqs. (5)-(11). In the case of anisotropic yield ratios were defined with respect to a reference yield stress σ^0 (the yield stress with a deposition direction of $0°$ (f_{y,s_0}) was defined as the reference yield stress σ^0 in this paper), as expressed in Eq. (12), such that if σ_{ij} is applied as the only nonzero stress, the corresponding yield stress is $R_{ij}f_{y,s\_0}$ or $R_{ij}f_{y,s\_0}/\sqrt{3}$. It should be noted that anisotropic yield stress ratios R_{ij} must be positive in Hill's potential function, thus the yield function is always well-defined. Therefore, the constitutive model of printed steel was defined as Hill's potential

function associated with the flow rule with isotropic strain hardening, which was determined by the measured stress-strain relationship of the WAAM tensile coupon.

The bilinear plus nonlinear hardening model by Eq. (13), which was typically used to capture the rounded stress-strain response of carbon steel [54], was employed for modelling the material response of the WAAM steel tube. In Eq. (13), σ and ε is the engineering stress and strain respectively; $\varepsilon_y = f_y/E_s$ is the yield strain; $\varepsilon_u = 0.6(1 - f_y/f_u)$ is the ultimate tensile strain; $\varepsilon_{sh} = 0.1 f_y/f_u - 0.055$ is the strain hardening strain. For input into the developed solid FE model [41], the engineering stresses and strains were converted into true stresses and strains. Meanwhile, material anisotropy was accounted for, both in the elastic and plastic material range, through use of the *Engineering Constants and *Potential keywords [41] respectively. Residual stresses and material defects, beyond those implicitly incorporated in the tensile coupons, i.e. the initial imperfection of scanned steel tube, have already been accounted for in the FE model.

$$f(\varepsilon) = \begin{cases} E_s\varepsilon & \text{for } \varepsilon \leq \varepsilon_y \\ f_y & \text{for } \varepsilon_y \leq \varepsilon \leq \varepsilon_{sh} \\ f_y + \left(f_u - f_y\right)\left\{0.4\left(\dfrac{\varepsilon - \varepsilon_{sh}}{\varepsilon_u - \varepsilon_{sh}}\right) + 2\left(\dfrac{\varepsilon - \varepsilon_{sh}}{\varepsilon_u - \varepsilon_{sh}}\right) \middle/ \left[1 + 400\left(\dfrac{\varepsilon - \varepsilon_{sh}}{\varepsilon_u - \varepsilon_{sh}}\right)^5\right]^{0.2}\right\} & \text{for } \varepsilon_{sh} \leq \varepsilon \leq \varepsilon_u \end{cases} \tag{13}$$

Table 4
Comparison of specimen strengths obtained from tests, numerical analyses and design equations.

Axial compressive specimens	$N_{u,Exp}$ (kN)	β	$\dfrac{N_{u,FE}}{N_{u,Exp}}$	GB 50936 $\dfrac{N_{u,FE}}{N_{u,GB}}$	AISC 360–16 $\dfrac{N_{u,FE}}{N_{u,AISC}}$	EC4 $\dfrac{N_{u,FE}}{N_{u,EC4}}$	AS 5100 $\dfrac{N_{u,FE}}{N_{u,AS}}$	ACI318 $\dfrac{N_{u,FE}}{N_{u,ACI}}$	BS5400 $\dfrac{N_{u,FE}}{N_{u,BS}}$	AIJ2001 $\dfrac{N_{u,FE}}{N_{u,AIJ}}$	Proposed design $\dfrac{N_{u,FE}}{N_{u,Design\_L}}$	$\dfrac{N_{u,FE}}{N_{u,Design\_M}}$	$\dfrac{N_{u,FE}}{N_{u,Design\_U}}$
D180T3L600	1904	0.78	0.96	0.96	1.31	1.08	1.13	1.34	1.27	1.29	1.1	1.08	1.06
D240T3L600	3010	0.77	0.97	0.97	1.40	1.09	1.07	1.35	1.29	1.34	1.11	1.09	1.06
D300T3L600	4274	0.74	0.97	0.99	1.54	1.06	1.05	1.35	1.32	1.37	1.08	1.07	1.04
D180T6L600	2428	0.91	1.02	0.93	1.24	1.00	1.05	1.25	1.06	1.10	1.05	1.03	1.01
D240T6L600	3797	0.92	1.02	0.92	1.27	1.03	1.02	1.31	1.10	1.19	1.02	1.01	0.98
D300T6L600	5460	0.88	0.99	0.91	1.26	1.00	0.99	1.31	1.12	1.23	0.99	0.97	0.94
D180T4L1200	2002	0.80	0.95	0.98	1.42	1.02	1.19	1.26	1.26	1.19	1.11	1.1	1.09
D240T4L1200	3208	0.81	0.98	0.97	1.44	1.06	1.14	1.31	1.28	1.27	1.12	1.1	1.08
D300T4L1200	4791	0.78	0.97	1.02	1.55	1.11	1.14	1.37	1.36	1.37	1.12	1.1	1.08
		Mean	0.98	0.96	1.38	1.05	1.09	1.32	1.23	1.26	1.08	1.06	1.04
		CoV	0.025	0.037	0.085	0.039	0.062	0.031	0.086	0.073	0.044	0.044	0.049

The plasticity behaviour of the confined concrete was determined by five plasticity parameters [55,56] and the uniaxial stress-strain relationships [57,58]. f_c was used in defining the uniaxial compressive stress-strain relationship by the confined concrete constitutive model suggested by Saenz [57] before f_c and Han et al. [58] for the post-peak stage, as expressed in Eqs. (14) and (15). $\varepsilon_{c,c} = 0.003(1 + 20.5 f_l/f_c)$ is the axial strain of confined concrete at f_c; f_l is the lateral confining pressure, as expressed in Eq. (16); $f_{ck} = 0.67 f_{cu}$ is the characteristic strength of the concrete; the elastic modulus and Poisson's ratio of concrete were taken as $E_c = 4730\sqrt{f_c}$ [59] and 0.2. For the uniaxial tensile stress-strain behaviour of concrete, a linear relationship was adopted before reaching the tensile strength $f_t = 0.3(0.67 f_{cu})^{2/3}$ [60], and the tension-softening behaviour was determined using the fracture-energy-based cracking criterion by directly defining the fracture energy value $G_F = 73(f_{ck} + 8)^{0.18}$ [60].

$$\sigma_c(\varepsilon) = \frac{E_c \varepsilon}{1 + \left(\frac{4E_c\,\varepsilon_{c,c}}{3f_c} - \frac{9}{4}\right)\left(\frac{\varepsilon}{\varepsilon_{c,c}}\right) - \left(2\frac{E_c\,\varepsilon_{c,c}}{3f_c} - \frac{3}{2}\right)\left(\frac{\varepsilon}{\varepsilon_{c,c}}\right)^2 + \left(\frac{E_c\,\varepsilon_{c,c}}{3f_c} - \frac{1}{4}\right)\left(\frac{\varepsilon}{\varepsilon_{c,c}}\right)^3}$$

(14)

$$\sigma_{c,post}(\varepsilon) = f_c \frac{\varepsilon/\varepsilon_{c,c}}{\left[(f_c)^{0.5} \times \left(2.36 \times 10^{-5}\right)^{\left[0.25 + \left(A_s f_y / A_c f_{ck} - 0.75\right)^7\right]}\right]\left(\varepsilon/\varepsilon_{c,c} - 1\right)^2 + \varepsilon/\varepsilon_{c,c}}$$

(15)

$$f_l = \begin{cases} (0.043646 - 0.000832\,(D/T)) f_y & 21.7 \le D/T \le 47 \\ (0.006241 - 0.0000357\,(D/T)) f_y & 47 < D/T \le 150 \end{cases}$$

(16)

3.2. Validations

The comparison of the load-displacement curves obtained from the test and FE analysis is presented in Fig. 6. The failure modes of specimens obtained by the developed FE models were compared with the test results, as shown in Fig. 7. Table 4 compares the axial compressive strengths of CFST specimens between the test and FE analysis. The average value and coefficient of variation (CoV) of $N_{u,FE}/N_{u,Exp}$ were 0.98 and 0.025, respectively. The FE results follow the trends observed in the physical testing, yielding accurate predictions of the experimental results. This indicates that the FE model of reverse reconstruction, which was established by real surface morphology, could satisfactorily simulate the axial compressive strength and failure mode of the specimens.

4. Analysis of numerical results

4.1. Composite action analysis

4.1.1. Stress nephogram

Fig. 13 shows the stress nephogram of steel tube and concrete elements at the mid-section and two end sections for D180T3L600 and D240T4L1200 specimen models obtained from FE analysis, in which the von Mises stress was used as the equivalent stress for determining the yield state of the WAAM tube, whilst the maximum principal stress was used as the equivalent stress for determining the damage state of concrete.

It is shown that the stresses of the concrete and steel elements at the mid-section are more uniform than those at the two end sections. This may be attributed to the compressive expansion of the concrete is easier to catch up with that of the steel tube in the mid-section, resulting in a stronger confinement effect of the steel tube in this location. Therefore, the concrete elements at this position are in a state of triaxial stress, leading to more uniform stress on it. On the other hand, the non-uniform stress distribution on the two end sections for inner concrete is also related to the influence of the load applied to the specimen, i.e. Saint Venant's principle. In addition, the non-uniform stresses on the steel section at two ends indicate that the geometric fluctuations of the WAAM steel tube will lead to the uneven confinement effect provided by the steel tube to the inner concrete.

Generally, the stress distributions on concrete and steel elements at the mid-section are very stable for the study of the compressive design of the concrete-filled WAAM steel tube.

4.1.2. Stress-strain curve

The longitudinal and circumferential stresses ($\sigma_{s,L}$ and $\sigma_{s,\theta}$) of the steel tube as well as the longitudinal stress (σ_c) of the inner concrete can reflect the intensity of the confinement effect of steel tube provided to concrete. With the increase of the circumferential stress of the steel tube, the longitudinal stress of the inner concrete will be improved, resulting in the strengthened confinement of the steel tube on the inner concrete. Therefore, the stresses of steel tube and concrete were obtained from the FE models of the CFST specimens at the mid-section. Noting that the compressive behaviours in this paper were taken as positive, and the circumferential stress should be negative.

The absolute value of longitudinal and circumferential stresses of the steel tube as well as the stress ratios of concrete against the longitudinal strain are shown in Fig. 14. It can be found that when the strain is less than approximately 0.02, the circumferential stress of steel element increases with the increase of strain, whilst the longitudinal stresses of the steel tube and concrete increases linearly and then decreases as the longitudinal strain. Within the strain range of 0.003–0.01, approximately, the transverse to longitudinal stress ratio increases and the
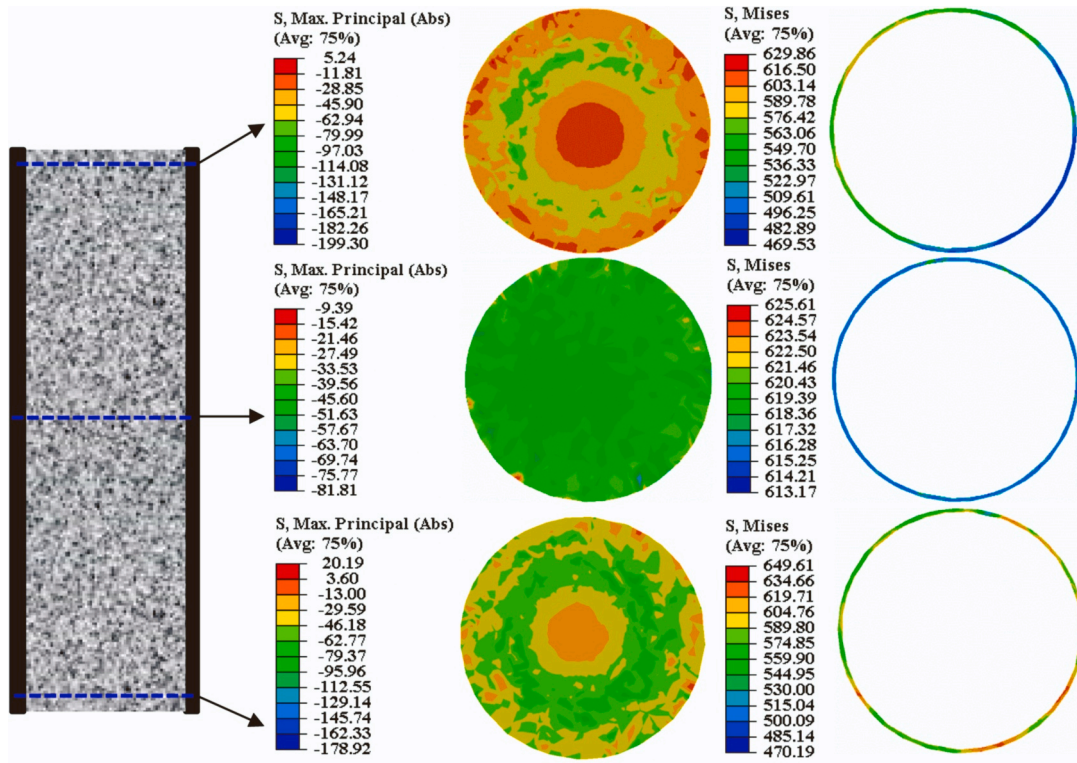
(a) D180T3L600
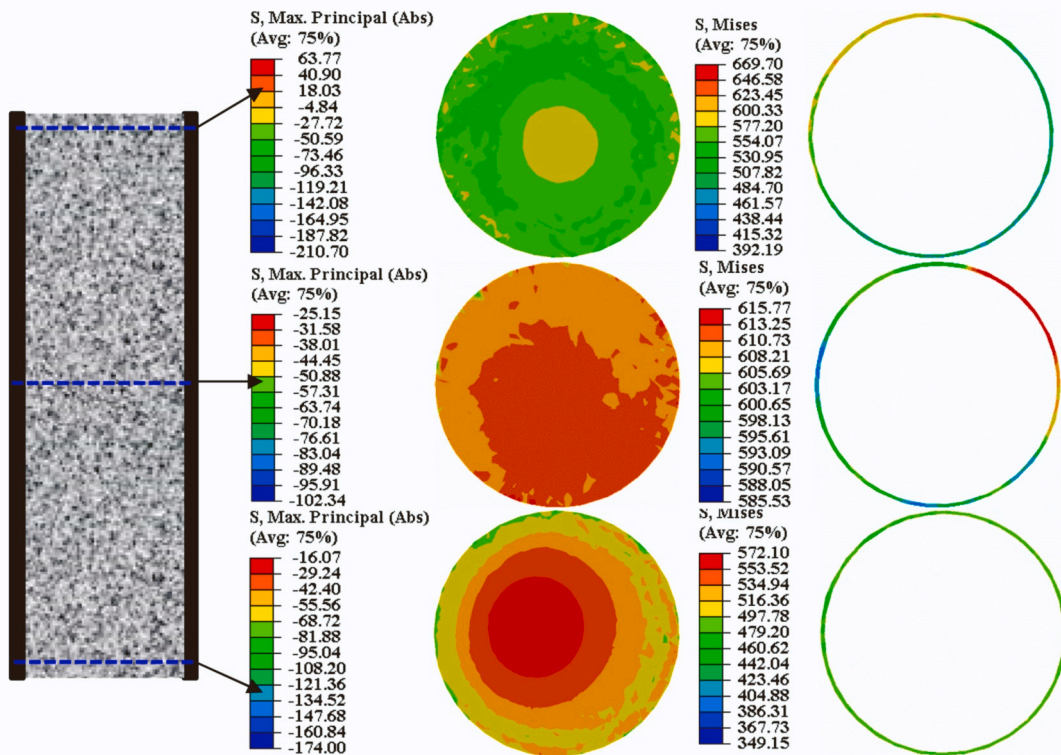
(b) D240T4L1200

Fig. 13. Stress nephogram of steel tube and inner concrete elements.
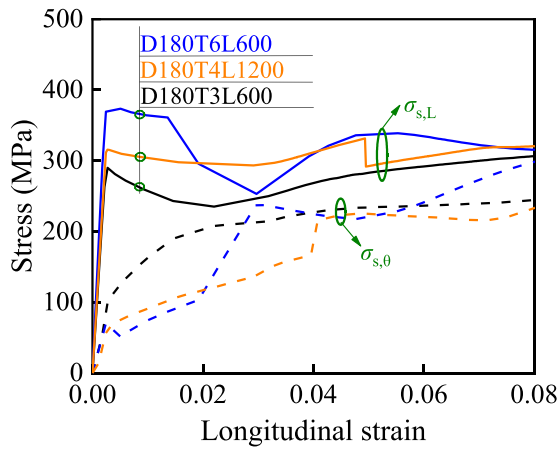
(a) Steel stress of D180 series
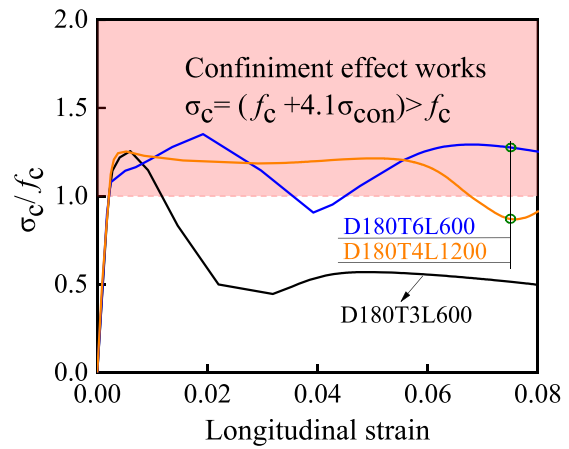
(b) Concrete stress ratio of D180 series
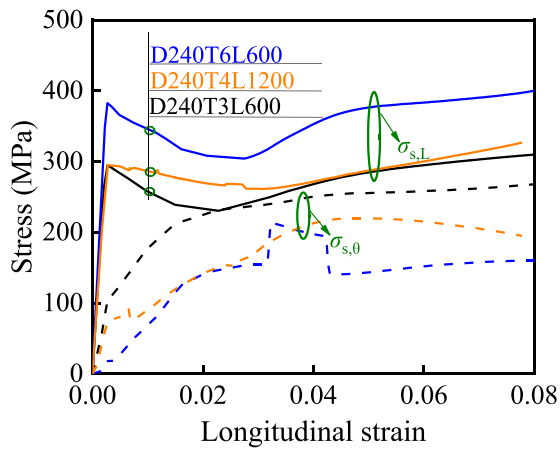
(c) Steel stress of D240 series
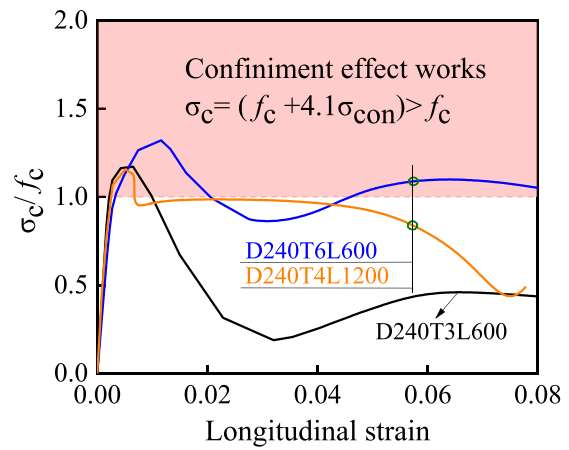
(d) Concrete stress ratio of D240 series
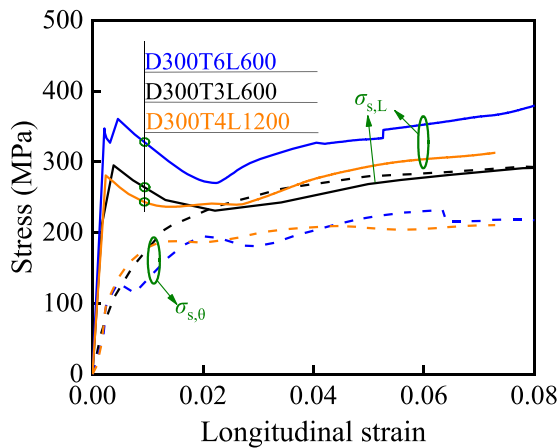
(e) Steel stress of D300 series
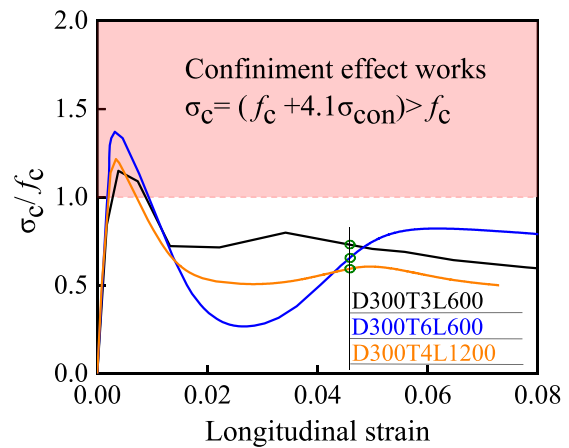
(f) Concrete stress ratio of D300 series

Fig. 14. Stress-strain relationship of steel element.

longitudinal stress of concrete is greater than the compressive strength of concrete. These indicate that the confinement effect ($4.1\sigma_{con}$) from the steel tube to the inner concrete continues to work at this stage, in which σ_{con} is the confining stress provided by the steel tube. Therefore, the composite action between the steel tube and inner concrete should be considered with great emphasis within the strain range of 0.003–0.01, approximately, for the concrete-filled WAAM steel tube. For a few

individual specimens, such as D180T6L600, D180T4L1200 and D240T6L600, the longitudinal stress ratio of concrete is still greater than 1 after the strain range. This is attributed to the fact that when the diameter-to-thickness ratio (D/T) of the steel tube is small enough, the longer the confinement effect lasts.

(a) Longitudinal stress ratio of steel tube

(b) Circumferential stress ratio of steel tube

(c) Longitudinal stress ratio of inner concrete

(d) Strength index *SI* of column
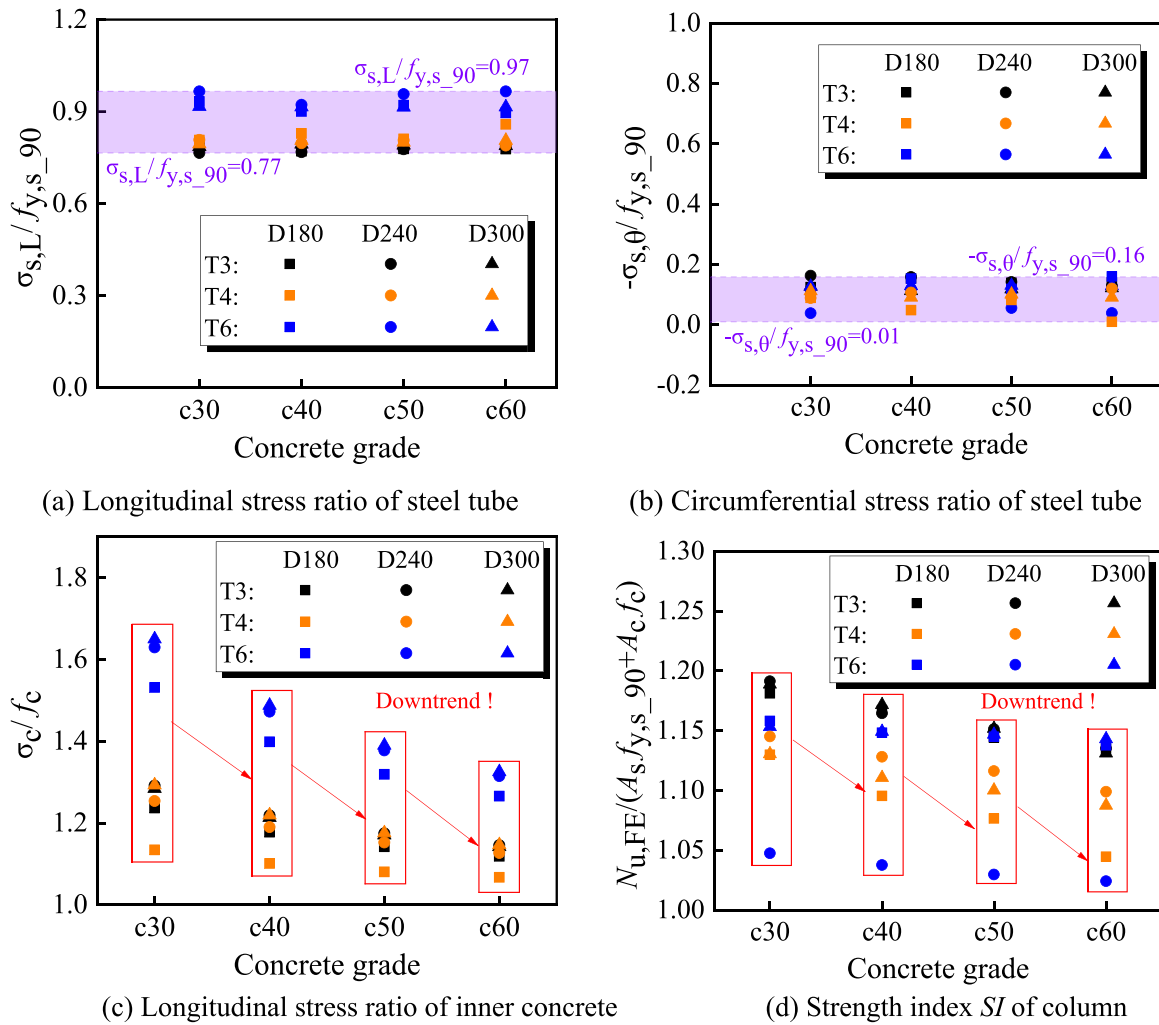
Fig. 15. The influence of concrete strength on the mechanical behaviour of column.

4.2. Parametric analysis

According to the confinement factor $f_{y,s}A_s/f_cA_c$ of concrete-filled conventional steel tubular members from the design code of GB50936–2014 [61], it can be seen that the material strengths and cross-sectional areas of steel and concrete exhibit a direct effect on the composite action between the steel tube and inner concrete. Therefore, the influences of the strengths of steel and concrete on the confinement effect provided by the WAAM steel tube to the inner concrete were parametrically studied for the concrete-filled WAAM steel tube member in this Section. Note that the effect of the cross-sectional area of steel tube and concrete on the confinement effect of the concrete-filled WAAM steel tube member will not be discussed in this paper. This is because the cross-sectional area of the WAAM steel tube is related to their thickness and size, but the data cannot be changed in existing models. In addition, the models in the parametric study were built with the same boundary conditions as the test specimens, and the same element type and numbers for the steel and concrete as the verified FE models. The yield strength ratios ($f_{y,s\_0} / f_{y,s\_90}$) of the WAAM steel tubes with a deposition direction of 0° –90° were kept the same with the CFST specimens.

4.2.1. Effect of concrete strength

To further explore the influence of concrete strength on the confinement effect of concrete-filled WAAM steel tube under axial compression, parametric studies were performed including the

following parameters: the nominal yield stress f_{y,s_90} of steel tube with a deposition direction of 90° was 345 MPa with the yield ratio of 0.7; Young's elastic module of steel tube was 203 GPa; the compressive strength f_c of concrete was 30 MPa, 40 MPa, 50 MPa, 60 MPa, respectively. The reverse reconstruction FE models of specimens were used again in the parametric study.

The average normalized stresses of steel tube and concrete at mid-section of the CFST columns as well as the strength indexes (*SI*) of the CFST columns are shown in Fig. 15. The stresses of steel tube and concrete are fetched when the CFST columns reach their compressive strength. It can be seen that the average normalized longitudinal stresses ($\sigma_{s,L}/f_{y,s\_90}$) of steel tube are within the range of 0.77–0.97, whilst the average normalized circumferential stresses ($\sigma_{s,\theta}/f_{y,s\_90}$) of steel tube are maintained at around 0.08, as shown in Fig. 15 (a) and (b). This indicates that the concrete strength exhibits little effect on the longitudinal $\sigma_{s,L}$ and circumferential $\sigma_{s,\theta}$ stresses of the WAAM steel tube. In addition, as illustrated in Fig. 15 (c), it can be found that the average normalized longitudinal stresses (σ_c/f_c) of inner concrete decrease as concrete strength increases. Meanwhile, as concrete strength increases, the compressive strength indexes of the CFST column have the same downward trend, as presented in Fig. 15 (d). These demonstrate that the confinement effect of the WAAM steel tube on inner concrete is weakened as the concrete strength increases.

In general, the concrete strength exhibits a negative impact on the confinement effect provided by the WAAM steel tube to the inner concrete but has a minor influence on the biaxial stresses of the WAAM steel

(a) Longitudinal stress ratio of steel tube

(b) Circumferential stress ratio of steel tube

(c) Longitudinal stress ratio of inner concrete

(d) Strength index *SI* of column
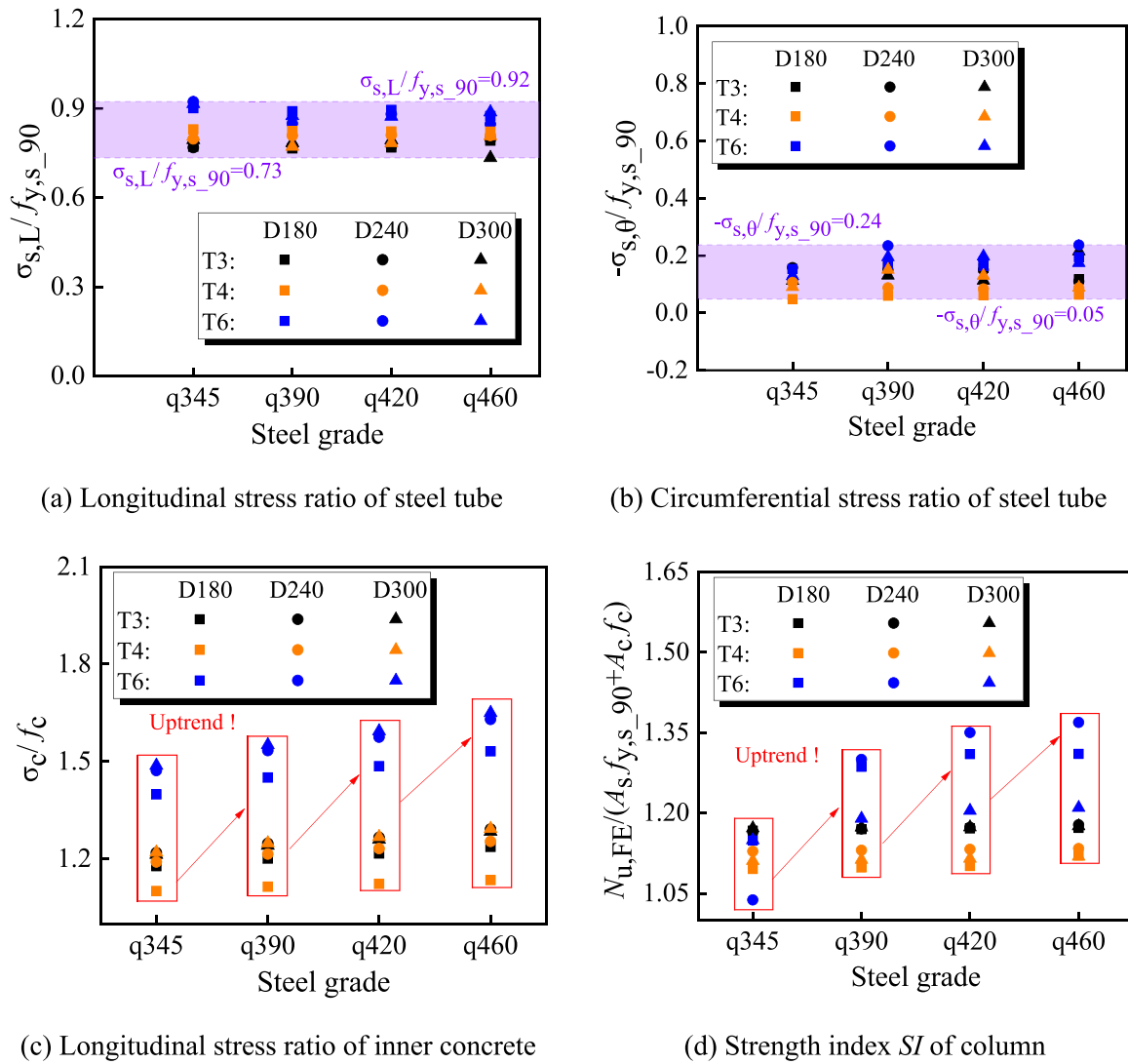
Fig. 16. The influence of steel strength on the mechanical behaviour of column.

tube when the CFST column reaches compressive strength.

4.2.2. Effect of steel strength

The influence of steel strength on the confinement effect of concrete-filled WAAM steel tube under axial loading was parametrically studied including the following parameters: the compressive strength f_c of concrete was 40 MPa; the nominal yield stresses f_{y,s_90} of steel tube with a deposition direction of 90° was 345 MPa, 390 MPa, 420 MPa, 460 MPa with the yield ratio of 0.7, respectively; Young's elastic module of steel tube was 203 GPa.

The average normalized stresses of steel tube and concrete at mid-section of the CFST columns as well as the strength indexes (*SI*) of the CFST columns are shown in Fig. 16. The stresses of steel tube and concrete were obtained when the CFST columns reach their compressive strength. It can be seen that the average normalized longitudinal stresses ($\sigma_{s,L}/f_{y,s\_90}$) of steel tube are stable within the range of 0.73–0.92, whilst the average normalized circumferential stresses ($\sigma_{s,\theta}/f_{y,s\_90}$) of steel tube are maintained at around 0.15, as shown in Fig. 16 (a) and (b). This indicates a positive correlation between the steel strength and the longitudinal $\sigma_{s,L}$ and circumferential $\sigma_{s,\theta}$ stresses of the WAAM steel tube, respectively. In addition, as illustrated in Fig. 16 (c), it can be found that the average normalized longitudinal stresses (σ_c/f_c) of inner concrete increase as steel strength increases. Meanwhile, as steel strength increases, the compressive strength indexes of the concrete-filled WAAM

steel tube still have an upward trend as shown in Fig. 16 (d). These demonstrate that the confinement effect of the WAAM steel tube on the inner concrete is strengthened as the steel strength increases.

In summary, the steel strength exhibits a positive impact on the confinement effect provided by the WAAM steel tube to the inner concrete when the CFST column reaches compressive strength.

5. Design recommendations of concrete-filled WAAM steel tube

5.1. Current design for CFST columns

The FE results were compared with the current design standards such as GB 50936 [61], AISC 360–16 [9], EC4 [62], AS 5100 [63], ACI318 [59], BS 5400 [64] and AIJ [65], as presented in Table 4. The predictions were calculated by the design formulas in those design codes using the average geometric dimensions and material properties of the concrete-filled WAAM steel tube. Comparison results demonstrate that the axial compressive strength design equations in design codes of GB 50936 and EC4 can reasonably well predict the ultimate strength of the concrete-filled WAAM steel tube with mean values of $N_{u,FE}/N_{u,GB}$ and $N_{u,FE}/N_{u,EC4}$ being 0.96 and 1.05, respectively. The predictions calculated by the design equation in AS 5100 are somewhat conservation with mean values of $N_{u,FE}/N_{u,AS}$ being 1.09. In addition, the predictions calculated by the design equations in standards of AISC 360–16, ACI318,
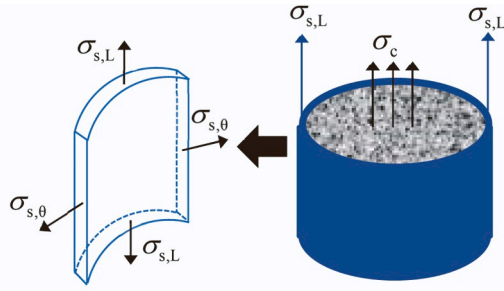
(a) Stress of each component
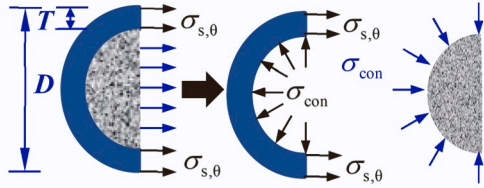
(b) Confinement stress of concrete provided by steel tube

Fig. 17. Stress state of steel tube and inner concrete under axial compression.
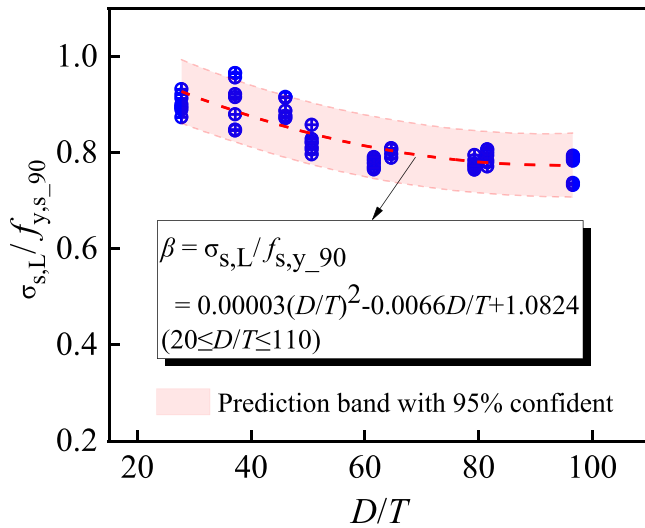
Fig. 18. Regression analysis of the coefficient β.

BS 5400 and AIJ are quite conservative.

Although GB 50936, EC4 and AS 5100 can predict the compressive strength of the CFST specimens within a relatively reasonable range, their prediction accuracy still varies, i.e. the Cov of $N_{u,FE}/N_{u,GB}$, $N_{u,FE}/N_{u,EC4}$ and $N_{u,FE}/N_{u,AS}$ being 0.037, 0.039 and 0.062. This is attributed to the geometric undulations and material anisotropy of the WAAM steel tube. Therefore, they shall be taken into account for the design methods of the compressive strength for the CFST specimens.

5.2. Proposed design method

5.2.1. General

The formulas for calculating the axial compressive strength of conventional CFST columns in GB 50936, EC4 and AS 5100 have a common characteristic, i.e. there is always a coefficient α_{sc} next to the cross-sectional resistance term of inner concrete $f_c A_c$. Although the coefficients α_{sc} are defined as different forms in different design codes [61–63], the fundamental principle is the same, i.e. the confinement

effect of the steel tube on the inner concrete. Thus, the formulas for calculating the axial compressive strength from GB 50936, EC4 and AS 5100 can predict the compressive strength of CFST specimens with reasonable accuracy because the confinement effect can be properly considered in those formulas. However, as mentioned in Section 5.1, the geometric undulations and material anisotropy of the used WAAM steel tube cannot be ignored, especially for the WAAM steel tube that directly provides a confinement effect for inner concrete. Therefore, the coefficient α_{sc} urgently needs to be redefined for the concrete-filled WAAM steel tube column in this paper.

5.2.2. Confinement effect based on the biaxial stress

In the initial stages of loading of the concrete-filled WAAM steel tube column subjected to axial compression, Poisson's ratio for the inner concrete was lower than that for the WAAM steel tube, therefore a separation between part of the steel tube wall and inner concrete took place. The longitudinal strain of the column reached the critical strain with an increase in the load applied in the column, resulting in the compressive expansion of the inner concrete in contact with that of the WAAM steel tube. After that, a tensile circumferential stress was developed in the steel tube, which led to the inner concrete being in a state of triaxial compression, as shown in Fig. 17(a), resulting in an increase of the axial compressive strength of the concrete-filled WAAM steel tube under axial compression.

Based on the above analysis, the design method for the compressive strength of concrete-filled WAAM steel tube columns under axial compression is obtained by the following procedure. The stress σ_c of confined concrete in the WAAM steel tube is assumed to be given by Eq. (17) [36,66]:

$$\sigma_c = f_c + 4.1\sigma_{con} \tag{17}$$

where σ_{con} is the confining stress provided by the WAAM steel tube. As mentioned in Section 4.2, a positive correlation between the steel strength and the longitudinal $\sigma_{s,L}$ and circumferential $\sigma_{s,\theta}$ stresses of the WAAM steel tube, respectively, can be found in the results of the parametric analysis. Moreover, the concrete strength has a minor influence on the biaxial stresses of the WAAM steel tube when the concrete-filled WAAM steel tube reaches its compressive strength. The biaxial stresses of the WAAM steel tube when the column reaches its compressive strength, therefore, can be assumed as expressed in Eq. (18):

$$\sigma_{s,L} = \beta f_{y,s\_90} , \quad \sigma_{s,\theta} = \alpha f_{y,s\_90} \tag{18}$$

where $\sigma_{s,L}$ and $\sigma_{s,\theta}$ is the longitudinal and circumferential stresses of steel tube, respectively, as shown in Fig. 17(a); α and β are the coefficients to be independent of material properties of the concrete-filled WAAM steel tube members. The coefficients α and β in the steel stress assumption at the ultimate state of the concrete-filled WAAM steel tube member must satisfy Hill's potential function (a simple extension of the von Mises yield criterion for considering material anisotropy of the used WAAM steel tube), as expressed in Eq. (19).

$$f(\sigma)^2 = F(\sigma_{s,\theta})^2 + G(\sigma_{s,L})^2 + H(\sigma_{s,L} - \sigma_{s,\theta})^2 \tag{19}$$

$$f(\sigma)^2 = \min(f_{y,s\_90}{}^2, f_{y,s\_0}{}^2) \tag{20}$$

$$F = \frac{1}{2}\left[1 + 1 - \frac{1}{(f_{y,s\_90}/f_{y,s\_0})^2}\right] \tag{21}$$

$$G = H = \frac{1}{2}\left[1 + \frac{1}{(f_{y,s\_90}/f_{y,s\_0})^2} - 1\right] \tag{22}$$

$$\gamma = \frac{f_{y,s\_0}}{f_{y,s\_90}} \tag{23}$$

Table 5
Comparison of FE model strengths obtained from numerical analyses and design equations.

Axial compressive specimens	f_{y,s_90} (MPa)	f_{cu} (MPa)	β	α_{sc}	$N_{u,FE}$ (kN)	GB 50936	EC4	AS 5100	Proposed design		
						$\dfrac{N_{u,FE}}{N_{u,GB}}$	$\dfrac{N_{u,FE}}{N_{u,EC4}}$	$\dfrac{N_{u,FE}}{N_{u,AS}}$	$\dfrac{N_{u,FE}}{N_{u,Design\_L}}$	$\dfrac{N_{u,FE}}{N_{u,Design\_M}}$	$\dfrac{N_{u,FE}}{N_{u,Design\_U}}$
D180T3L600-C30	345	30	0.79	1.24	1309	0.91	0.98	1.01	1.08	1.05	1.03
D240T3L600-C30	345	30	0.76	1.29	2118	0.92	0.99	0.98	1.04	1.02	0.99
D300T3L600-C30	345	30	0.79	1.28	3023	0.92	0.97	0.96	1.02	1.01	0.99
D180T6L600-C30	345	30	0.93	1.53	1988	0.98	0.97	0.99	1.02	1.00	0.98
D240T6L600-C30	345	30	0.97	1.63	2687	0.86	0.85	0.84	0.86	0.85	0.83
D300T6L600-C30	345	30	0.92	1.65	4122	0.93	0.91	0.90	0.92	0.90	0.88
D180T4L1200-C30	345	30	0.81	1.13	1387	0.87	0.93	1.07	1.09	1.06	1.05
D240T4L1200-C30	345	30	0.81	1.25	2237	0.88	0.96	1.02	1.06	1.01	0.99
D300T4L1200-C30	345	30	0.79	1.29	3130	0.87	0.96	0.97	1.01	0.97	0.94
D180T3L600-C40	345	40	0.77	1.18	1511	0.90	0.99	1.02	1.08	1.06	1.04
D240T3L600-C40	345	40	0.77	1.22	2464	0.90	1.00	0.99	1.04	1.02	1.00
D300T3L600-C40	345	40	0.79	1.21	3595	0.91	1.00	0.99	1.03	1.02	1.00
D180T6L600-C40	345	40	0.90	1.40	2169	0.96	0.98	1.00	1.02	1.00	0.98
D240T6L600-C40	345	40	0.92	1.47	2993	0.84	0.87	0.86	0.87	0.86	0.84
D300T6L600-C40	345	40	0.91	1.49	4694	0.92	0.94	0.93	0.94	0.92	0.90
D180T4L1200-C40	345	40	0.83	1.10	1548	0.84	0.92	1.05	1.06	1.04	1.02
D240T4L1200-C40	345	40	0.80	1.19	2584	0.87	0.96	1.03	1.05	1.01	1.00
D300T4L1200-C40	345	40	0.81	1.22	3667	0.86	0.97	0.98	1.01	0.97	0.95
D180T3L600-C50	345	50	0.78	1.14	1695	0.88	0.99	1.03	1.07	1.05	1.03
D240T3L600-C50	345	50	0.78	1.17	2825	0.89	1.02	1.00	1.04	1.03	1.01
D300T3L600-C50	345	50	0.79	1.17	4139	0.90	1.01	1.00	1.03	1.02	1.01
D180T6L600-C50	345	50	0.92	1.32	2360	0.95	0.98	1.02	1.03	1.01	0.99
D240T6L600-C50	345	50	0.96	1.38	3299	0.83	0.88	0.87	0.88	0.87	0.85
D300T6L600-C50	345	50	0.91	1.39	5269	0.92	0.97	0.95	0.95	0.94	0.92
D180T4L1200-C50	345	50	0.81	1.08	1721	0.83	0.92	1.05	1.05	1.03	1.01
D240T4L1200-C50	345	50	0.81	1.15	2933	0.86	0.97	1.04	1.05	1.02	1.00
D300T4L1200-C50	345	50	0.80	1.18	4219	0.85	0.98	1.00	1.01	0.98	0.96
D180T3L600-C60	345	60	0.78	1.12	1893	0.88	1.00	1.04	1.07	1.05	1.04
D240T3L600-C60	345	60	0.78	1.15	3169	0.88	1.02	1.01	1.04	1.03	1.01
D300T3L600-C60	345	60	0.79	1.14	4659	0.88	1.01	1.00	1.03	1.02	1.00
D180T6L600-C60	345	60	0.90	1.27	2541	0.94	0.99	1.02	1.03	1.01	1.00
D240T6L600-C60	345	60	0.97	1.31	3608	0.82	0.90	0.88	0.88	0.87	0.86
D300T6L600-C60	345	60	0.91	1.33	5835	0.91	0.98	0.97	0.97	0.96	0.94
D180T4L1200-C60	345	60	0.86	1.07	1864	0.81	0.91	1.03	1.02	1.00	0.99
D240T4L1200-C60	345	60	0.79	1.13	3258	0.85	0.97	1.03	1.04	1.01	1.00
D300T4L1200-C60	345	60	0.81	1.15	4750	0.85	0.98	1.00	1.01	0.98	0.97
D180T3L600-Q390	390	40	0.77	1.20	1598	0.89	0.99	1.02	1.08	1.05	1.03
D240T3L600-Q390	390	40	0.77	1.25	2593	0.90	1.00	0.99	1.03	1.02	0.99
D300T3L600-Q390	390	40	0.78	1.24	3747	0.90	0.99	0.98	1.02	1.01	0.99
D180T6L600-Q390	390	40	0.89	1.45	2631	1.10	1.09	1.13	1.14	1.12	1.09
D240T6L600-Q390	390	40	0.85	1.53	4022	1.06	1.09	1.07	1.08	1.07	1.04
D300T6L600-Q390	390	40	0.87	1.55	5176	0.95	0.97	0.96	0.96	0.95	0.92
D180T4L1200-Q390	390	40	0.82	1.11	1648	0.84	0.91	1.06	1.06	1.04	1.02
D240T4L1200-Q390	390	40	0.81	1.22	2728	0.86	0.96	1.03	1.05	1.01	0.99
D300T4L1200-Q390	390	40	0.77	1.25	3844	0.85	0.96	0.98	1.01	0.96	0.94
D180T3L600-Q420	420	40	0.77	1.22	1656	0.89	0.98	1.02	1.07	1.05	1.03
D240T3L600-Q420	420	40	0.77	1.27	2677	0.89	1.00	0.98	1.03	1.01	0.99
D300T3L600-Q420	420	40	0.79	1.26	3847	0.90	0.99	0.97	1.02	1.01	0.98
D180T6L600-Q420	420	40	0.89	1.49	2816	1.13	1.10	1.15	1.16	1.13	1.11
D240T6L600-Q420	420	40	0.88	1.57	4366	1.10	1.13	1.12	1.11	1.10	1.07
D300T6L600-Q420	420	40	0.87	1.59	5454	0.96	0.98	0.97	0.97	0.95	0.93
D180T4L1200-Q420	420	40	0.82	1.12	1716	0.84	0.91	1.07	1.06	1.04	1.02
D240T4L1200-Q420	420	40	0.81	1.23	2825	0.86	0.95	1.03	1.05	1.01	0.99
D300T4L1200-Q420	420	40	0.78	1.27	3965	0.85	0.96	0.98	1.00	0.96	0.94
D180T3L600-Q460	460	40	0.79	1.24	1732	0.88	0.97	1.02	1.07	1.05	1.02
D240T3L600-Q460	460	40	0.80	1.29	2792	0.89	1.00	0.98	1.03	1.01	0.98
D300T3L600-Q460	460	40	0.73	1.28	3986	0.89	0.98	0.97	1.01	1.00	0.98
D180T6L600-Q460	460	40	0.87	1.53	2999	1.14	1.10	1.16	1.15	1.13	1.11
D240T6L600-Q460	460	40	0.85	1.63	4683	1.12	1.15	1.13	1.12	1.11	1.08
D300T6L600-Q460	460	40	0.89	1.65	5765	0.97	0.98	0.97	0.96	0.95	0.92
D180T4L1200-Q460	460	40	0.82	1.13	1834	0.85	0.92	1.09	1.08	1.06	1.04
D240T4L1200-Q460	460	40	0.81	1.25	2952	0.85	0.95	1.03	1.05	1.00	0.98
D300T4L1200-Q460	460	40	0.81	1.29	4130	0.84	0.95	0.98	1.00	0.96	0.93
					Mean	0.91	0.98	1.01	1.03	1.01	0.99
					CoV	0.084	0.057	0.062	0.060	0.060	0.061

where $F = (2 - \gamma^2)/2$ and $G = H = \gamma^2/2$ are constants obtained by tests of the material in different orientations, as expressed in Eqs. (21) to (23), in which γ is the ratio of the yield strength f_{y,s_0} to f_{y,s_90}; f_{y,s_90} and f_{y,s_0} is the yield strength of WAAM steel with a deposition direction of $90°$ and

$0°$, respectively. Rearranging Eqs. (18) and (23), the relationship of the coefficients α and β can be expressed in Eq. (20). Thus, the generalized von Mises yield criterion, i.e. Eq. (24), is always well-defined. Noting that the coefficient α is negative and the coefficient β is positive,

(a) Prediction of design codes (b) Prediction of the proposed design method
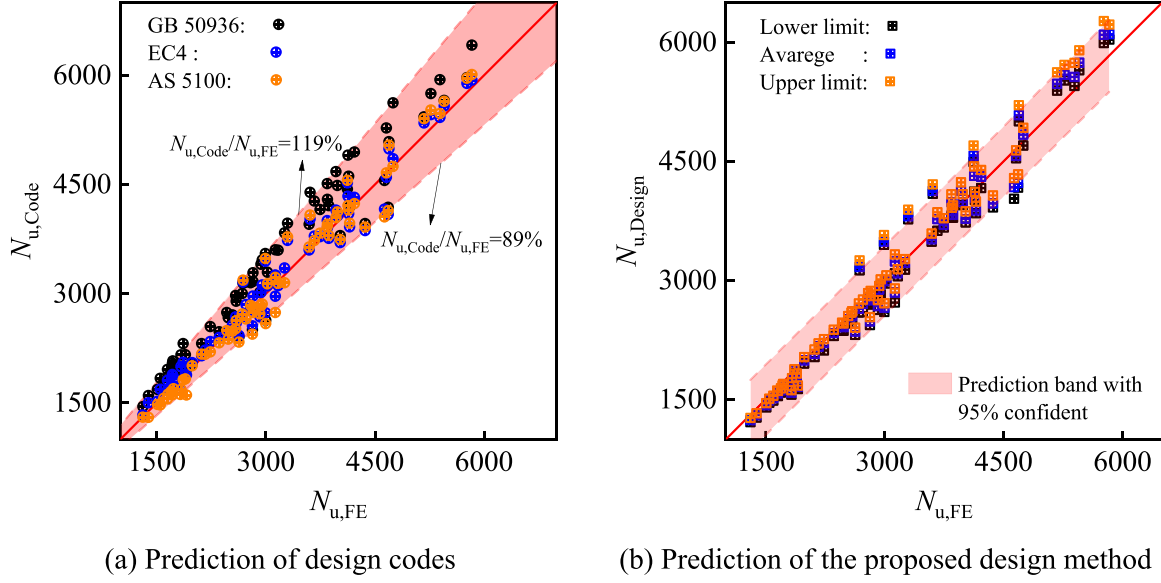
Fig. 19. Comparison between the compressive strength predictions from design codes, proposed design method and FE results.

$$\left(\gamma\sigma_{s,L}\right)^2 - \gamma^2\sigma_{s,L}\sigma_{s,\theta} + \sigma_{s,\theta}^2 = \left(\gamma\beta f_{y,s\_90}\right)^2 - \gamma^2\beta\alpha f_{y,s\_90}f_{y,s\_90} + \left(\alpha f_{y,s\_90}\right)^2$$
$$= \begin{cases} f_{y,s\_90}{}^2 (\gamma \geq 0) \\ f_{y,s\_0}{}^2 (\gamma < 0) \end{cases}$$

$$(24)$$

The yield strength of WAAM steel with a deposition direction of $0°$ is always greater than that of WAAM steel with a deposition direction of $90°$ in this paper. Therefore, from Eq. (24), the coefficient α can be calculated as follows:

$$\alpha = \frac{\gamma^2\beta - \sqrt{4 + \gamma^4\beta^2 - 4\gamma^2\beta^2}}{2} < 0 \tag{25}$$

Because the confinement stress of concrete σ_{con} is provided by the WAAM steel tube, as illustrated in Fig. 17 (b), the relation between the circumferential stresses of the WAAM steel tube $\sigma_{s,\theta}$ and the confinement stress of the inner concrete σ_{con} can be expressed as Eq. (26). It should be noted that positive values indicate the compressive behaviour in this paper.

$$\sigma_{con} = -\frac{2T}{D - 2T}\sigma_{s,\theta} \tag{26}$$

Rearranging Eqs. (17), (18), (25) and (26), the stress of confined concrete σ_c when the concrete-filled WAAM steel tube reaches its compressive strength can be expressed as follows:

$$\sigma_c = f_c \left(1 - 4.1\frac{2T}{D - 2T}\frac{\gamma^2\beta - \sqrt{4 + \gamma^4\beta^2 - 4\gamma^2\beta^2}}{2}\frac{f_{y,s\_90}}{f_c}\right) \tag{27}$$

It can be seen from Eq. (27) that the normalized longitudinal stress (σ_c/f_c) of inner concrete is positively correlated with steel strength and negatively correlated with concrete strength, which once again confirms the conclusion in parameter analysis.

5.2.3. Axial compressive strength considering the confinement effect

Based on the static equilibrium of the composite cross-section, the axial compressive strength as a composite section made of the WAAM steel tube and concrete, induced by confined stress can be given by method of Eq. (28) as below, in which α_{sc} is the confinement factor provided by the WAAM steel tube to the inner concrete, as expressed in Eq. (29):

$$N_{u,Design} = A_s f_{y,s\_90} + A_c \sigma_c = A_s f_{y,s\_90} + A_c f_c \alpha_{sc} \tag{28}$$

$$\alpha_{sc} = 1 - 4.1\frac{2T}{D - 2T}\frac{\gamma^2\beta - \sqrt{4 + \gamma^4\beta^2 - 4\gamma^2\beta^2}}{2}\frac{f_{y,s\_90}}{f_c} \tag{29}$$

The coefficient β can be determined by a regression analysis based on the numerical models as described in Section 4.2. Fig. 18 shows the ratio of the longitudinal stress $(\sigma_{s,L})$ of the WAAM steel tube in the mid-section to the yield stress (f_{y,s_90}) of the WAAM steel tube with a deposition direction of $90°$ against the diameter-to-thickness ratio (D/T). The best-fitting curves between the coefficient β and the diameter-to-thickness ratio D/T of a power relationship with 95% prediction bands are expressed in Eq. (30):

$$\beta = \frac{1}{25}\left(\frac{D}{100T}\right)^2 - \frac{33}{5000}\frac{D}{T} + 1.0824 \left(20 \leq \frac{D}{T} \leq 110\right) \tag{30}$$

It should be noted that the proposed equations, i.e. Eqs. (28) to (30) are validated within the range of the parametric study, i.e. 30 MPa $\leq f_{cu} \leq$ 60MPa , 345MPa $\leq f_{y,s\_90} \leq$ 460MPa and $20 \leq D/T \leq 110$. Noting that for Eq. (28), the concrete-filled WAAM steel tube member is considered as a stub column without considering the reduction factor for the buckling failure mode. If the buckling failure mode is involved in the failure of the CFST member, then it is necessary to further introduce relevant reduction factors based on Eq. (28).

5.2.4. Formula validation

Eq. (28) are used to predict 72 FE models in Section 4.2, and the predictions $N_{u,Design\_M}$ are compared with the results of the FE simulation, whilst the predictions of GB 50936 [61], EC4 [62] and AS 5100 [63] are also compared with corresponding FE results, as presented in Tables 4 and 5 and Fig. 19. It can be found that GB 50936, EC4 and AS 5100 can predict the compressive strength of the concrete-filled WAAM steel tube column within a reasonable range (−11% to 19%), as presented in Tables 4 and 5. Considering the effect of geometric undulations of the used WAAM steel tube, the upper limit of predictions $N_{u,Design\_U}$ and lower limit of predictions $N_{u,Design\_L}$ calculated based on the minimum and maximum dimensions of the WAAM steel tube, respectively, are compared with the FE results. It can be found that the proposed design equations (Eq. (28)) can predict the axial compressive strengths of concrete-filled WAAM steel tube columns with reasonable accuracy with 95% prediction bands. Furthermore, the compared results of the mean values of $N_{u,FE}/N_{u,Design\_U}$, $N_{u,FE}/N_{u,Design\_M}$ and $N_{u,FE}/N_{u,Design\_L}$ being 1.03, 1.01 and 0.99, respectively, and the CoV being 0.06, 0.06 and 0.061 once again prove the above

conclusion.

6. Conclusions

This paper investigated the structural behaviour of concrete-filled WAAM steel tubes under compressive load. According to the results of the experimental, numerical and theoretical studies, the following conclusions can be drawn:

(1) The experimental result shows that the ductility of concrete-filled WAAM steel tubes has some differences compared to that of concrete-filled conventional steel tubes.

(2) The developed FE models based on 3D models obtained by the 3D laser scan, which considers the material anisotropy of WAAM steel, are verified against the existing test results. The FE results indicate that the composite action should be significantly considered within the strain range of 0.003–0.01.

(3) The parametric study shows that the concrete and steel strength exhibit a negative and positive impact on the confinement effect, respectively, and the biaxial stress ratios of the WAAM steel tube are only related to the steel strength.

(4) The design method, which takes into account the influence of the geometric undulations and material anisotropy of the WAAM steel tube, is proposed based on the theory of confining effect, and the comparison results show that the comparison results show that the proposed method can predict the axial compressive strengths of the concrete-filled WAAM steel tubes with reasonable accurate.

CRediT authorship contribution statement

Sha-sha Song: Writing – original draft & editing, Methodology, Investigation. **Ju Chen**: Writing – review & editing, Supervision, Resources, Project administration, Funding acquisition, Conceptualization. **Jun Ye**: Methodology, Investigation, Writing – review & editing, Supervision, Resources, Project administration, Funding acquisition, Conceptualization. **Guan Quan**: Writing – review & editing, Writing, Supervision, Conceptualization. **Yang Zhao**: Writing – review & editing, Conceptualization.

Declaration of Competing Interest

There is no conflict of interest among the authors in the manuscript.

Data availability

Data will be made available on request.

Acknowledgements

References

[1] Colegrove PA, Coules HE, Fairman JL, Martina F, Kashoob T, Mamash H, Cozzolino LD. Microstructure and residual stress improvement in wire and arc additively manufactured parts through high-pressure rolling. J Mater Process Technol 2013;213:1782–91.

[2] Haden CV, Zeng G, Carter FMIII, Ruhl C, Krick BA, Harlow DG. Wire and arc additive manufactured steel: Tensile and wear properties. Addit Manuf 2017;16: 115–23.

[3] Müller J, Grabowski M, Müller C, Hensel J, Unglaub J, Thiele K, Kloft H, Dilger K. Design and parameter identification of wire and arc additively manufactured (WAAM) steel bars for use in construction. Metals 2019;9(7):1–19.

[4] Laghi V, Palermo M, Gasparini G, Girelli VA, Trombetti T. Experimental results for structural design of wire-and-arc additive manufactured stainless steel members. J Constr Steel Res 2020;16:105858.

[5] Kyvelou P, Slack H, Mountanou DD, Wadee MA, Britton TB, Buchanan C, Gardner L. Mechanical and micro-structural testing of WAAM sheet material. Mater Des 2020;192:108675.

[6] Kyvelou P, Huang C, Gardner L, Buchanan C. Structural testing and design of wire arc additively manufactured square hollow sections. J Struct Eng 2021;147(12): 04021218.

[7] Joosten SK. Printing a stainless steel bridge: An exploration of structural properties of stainless steel additive manufactures for civil engineering purposes. Delft Univ Technol, Ph D Thesis 2015.

[8] GB 50017. Code for Design of Steel Structures. Standards Press of China, Beijing, China; 2017. (in Chinese).

[9] AISC 360. Specification for structural steel buildings. AISC 360–16, Chicago; 2016.

[10] CEN (European Committee for Standardization). Eurocode 3: Design of Steel Structures. Part 1–8: Design of Joints. EN1993-1-8. Brussels, Belgium; 2007.

[11] AS4100. Build Code Aust Prim Ref Stand: Steel Struct Aust 1998.

[12] Gardner L, Kyvelou P, Herbert G, Buchanan C. Testing and initial verification of the world's first metal 3D printed bridge. J Constr Steel Res 2020;172:106233.

[13] Zhao Y, Chen Y, Wang Z, Ye J, Zhao WJ. Mechanical properties, microstructural characteristics and heat treatment effects of WAAM stainless-steel plate material. J Build Eng 2023;75:106988.

[14] Guo X, Kyvelou P, Ye J, Teh LH, Gardner L. Experimental investigation of wire arc additively manufactured steel single-lap shear bolted connections. Thin-Walled Struct 2022;181:110029.

[15] Guo X, Kyvelou P, Ye J, Teh TH, Gardner L. Experimental study of DED-arc additively manufactured steel double-lap shear bolted connections. Eng Struct 2023;281:115736.

[16] Guo X, Kyvelou P, Ye J, Gardner L. Experimental investigation of wire arc additively manufactured steel T-stub connections. J Constr Steel Res 2023;211: 108106.

[17] Buchanan C, Matilainen VP, Salminen A, Gardner L. Structural performance of additive manufactured metallic material and cross-sections. J Constr Steel Res 2017;136:35–48.

[18] Yan JJ, Chen MT, Quach WM, Yan M, Young B. Mechanical properties and cross-sectional behavior of additively manufactured high strength steel tubular sections. Thin-Walled Struct 2019;144:106158.

[19] Derazkolaa HA, Khodabakhshib F, Gerlichc AP. Fabrication of a nanostructured high strength steel tube by friction-forging tubular additive manufacturing (FFTAM) technology. J Manuf Process 2020;58:724–35.

[20] Zhang RZ, Gardner L, Meng X, Buchanan C, Matilainen VP, Piili H, Salminen A. Optimisation and compressive testing of additively manufactured stainless steel corrugated shells. ce/Pap 2021;4:1829–36.

[21] Ge HB, Usami T. Strength of concrete-filled thin-walled steel box columns: experiment. J Struct Eng 1992;118(11):3036–54.

[22] Han LH, Zhao XL, Yang YF, Feng JB. Experimental study and calculation of fire resistance of concrete-filled hollow steel columns. J Struct Eng 2003;129(3): 346–56.

[23] Zhou F, Young B. Concrete-filled aluminum circular hollow section column tests. Thin-Walled Struct 2009 2009;47(11):1272–80.

[24] Uy B. Strength of short concrete filled high strength steel box columns. J Constr Steel Res 2001;57:113–34.

[25] Han LH, Chen F, Liao FY, Tao Z, Uy B. Fire performance of concrete-filled stainless steel tubular columns. Eng Struct 2013;56:165–81.

[26] Chen J, Ni YY, Jin WL. Column tests of dodecagonal section double skin concrete-filled steel tubes. Thin-Walled Struct 2015;88:28–40.

[27] Aslani F, Uy B, Wang ZW, Patel V. Confinement models for high strength short square and rectangular concrete-filled steel tubular columns. Steel Compos Struct 2016;22(5):937–74.

[28] Tao Z, Katwal U, Uy B, Wang WD. Simplified nonlinear simulation of rectangular concrete-filled steel tubular columns. J Struct Eng 2021;147(6):1–19.

[29] Liang QQ, Uy B, Liew JYR. Nonlinear analysis of concrete-filled thin-walled steel box columns with local buckling effects. J Constr Steel Res 2006;62(6):581–91.

[30] Liang QQ, Fragomeni S. Nonlinear analysis of circular concrete-filled steel tubular short columns under axial loading. J Constr Steel Res 2009;65(12):2186–96.

[31] Han LH, Yao GH, Zhao XL. Tests and calculations for hollow structural steel (HSS) stub columns filled with self-consolidating concrete (SCC). J Constr Steel Res 2005; 61:1241–69.

[32] Uy B, Tao Z, Han LH. Behaviour of short and slender concrete-filled stainless steel tubular columns. J Constr Steel Res 2011;67(3):360–78.

[33] Tao Z, Han LH, Wang ZB. Experimental behaviour of stiffened concrete-filled thin-walled hollow steel structural (HSS) stub columns. J Constr Steel Res 2005;61: 962–83.

[34] Yu Q, Tao Z, Wu YX. Experimental behaviour of high performance concrete-filled steel tubular columns. Thin-Walled Struct 2008;46:362–70.

[35] Aslani F, Uy B, Tao Z, Mashiri F. Behaviour and design of composite columns incorporating compact high-strength steel plates. J Constr Steel Res 2015;107: 94–110.

[36] Xiong MX, Xiong DX, Liew JYR. Axial performance of short concrete filled steel tubes with high- and ultra-high-strength materials. Eng Struct 2017;136:494–510.

[37] Song S.S., Chen J., Ye J., Quan G., Wang Z., Xiao J.Z. Experimental study on the interfacial bond behaviour of circular concrete-filled WAAM steel tubes. Journal of Building Engineering, 2023 (submitted).

[38] Xu F, Chen J, Jin WL. Experimental investigation of thin-walled concrete-filled steel tube columns with reinforced lattice angle. Thin-Walled Struct 2014;84: 59–67.

[39] Xu F, Chen J, Guo Y, Ye Y. Innovative design of the world's tallest electrical transmission towers. Proc Inst Civ Eng – Civ Eng 2019;172(5):9–16.

[40] Chen J., Song S.S., Ye J., Quan G., Kyvelou P., Gardner L. Axial compressive behaviour and design of concrete-filled wire arc additively manufactured steel tubes. Structures 2023, (submitted).

[41] Abaqus/CAE, Dassault Systems Simulate Corp, 2016.

[42] Song SS, Xu F, Chen J, Qin FJ, Huang Y, Yan X. Feasibility and performance of novel tapered iron bolt shear connectors in demountable composite beams. J Build Eng 2022;53:104528.

[43] Song SS, Liu X, Chen J, Ye CH, Liu JDR, Liu CB. Compressive behaviour of corroded thin-walled circular section steel stub columns. Thin-Walled Struct 2022;180: 109794.

[44] Song SS, Chen J, Xu F. Mechanical behaviour and design of concrete-filled K and KK CHS connections. J Constr Steel Res 2022. 18833:10700.

[45] Ding FX, Luo L, Zhu J, et al. Mechanical behavior of stirrup-confined rectangular CFT stub columns under axial compression. Thin-Walled Struct 2018;124:136–50.

[46] Chen ZP, Liu DY, Liang YH, Zhou J. Experimental investigation on axial compression performance of spiral reinforcement ocean concrete-filled stainless steel tube columns. J Build Struct 2022. https://doi.org/10.14006/j. jzjgxb.2022.0401.

[47] Chen ZP, Jing CG, Ning F. Axial compressive behavior and parametric analysis of spiral reinforcement concrete filled square steel tubular columns. China Civ Eng J 2018;51(1):13–22.

[48] Chen ZP, Pang YS, Xu RT, Zhou J, Xu WS. Mechanical performance of ocean concrete-filled circular CFRP-steel tube columns under axial compression. J Constr Steel Res 2022;198:107514.

[49] Sakino K, Nakahare H, Morino S, Nishiyama I. Behavior of centrally loaded concrete-filled steel-tube short columns. J Struct Eng 2004;130(2):180–8.

[50] Xue JQ, Briseghella B, Chen BC. Effects of debonding on circular CFST stub columns. J Constr Steel Res 2012;69:64–76.

[51] Huang CS, Yeh YK, Liu GY, Hu HT, Tsai KC, Weng YT, Wang SH, Wu MH. Axial load behavior of stiffened concrete-filled steel columns. J Struct Eng 2002;128(9): 1222–30.

[52] Ding FX, Lu DR, Bai Y, Zhou QS, Ni M, Yu ZW, Jiang GS. Comparative study of square stirrup-confined concrete-filled steel tubular stub columns under axial loading. Thin-Walled Struct 2016;98:443–53.

[53] Rhinoceros 3D, Robert McNeel & Associates, 2017.

[54] Yun X, Gardner L. Stress-strain curves for hot-rolled steels. J Constr Steel Res 2017; 133:36–46.

[55] Xu F, Chen J, Chan TM. Numerical investigation on compressive performance of CFST columns with encased built-up lattice-angles. J Constr Steel Res 2017;137: 242–53.

[56] Tao Z, Wang ZB, Yu Q. Finite element modelling of concrete-filled steel stub columns under axial compression. J Constr Steel Res 2012;89:121–31.

[57] Saenz LP. Discussion of equation for the stress-strain curve of concrete by Desayi and Krishnan. J Am Concr Inst 1964;61:1229–35.

[58] Han LH, Yao GH, Tao Z. Performance of concrete-filled thin-walled steel tubes under pure torsion. Thin-Walled Struct 2007;45(1):24–36.

[59] ACI 318, Building code requirements for reinforced concrete and commentary, American Concrete Institute (ACI), Farmington Hill, Detroit, USA, 2011.

[60] CEB-FIP Model Code 2010, Fib model code for concrete structures 2010, federation internationale du beton (fib), Lausanne, Switzerland, 2012.

[61] GB 50936. Technical code for concrete-filled steel tubular structures. Standards Press of China, Beijing, China; 2014. (in Chinese).

[62] CEN (European Committee for Standardization). Eurocode 4: Design of composite steel and concrete structures-Part 1-1: General rules and rules for buildings. EN1994-1-1. Brussels, Belgium: CEN,; 2004.

[63] AS 5100. Bridge design Part 6: Steel and composite construction. Sydney, Australia; 2004.

[64] BS 5400. Steel, concrete and composite bridges: code of practice for design of composite bridges Part 5. London, British; 2000.

[65] AIJ 1997. Recommendations for design and construction of concrete filled steel tubular structures. Japan; 1997. (in Japanese).

[66] Uenaka K. Experimental study on concretefilled elliptical/oval steel tubular stub columns under compression. Thin-Walled Struct 2014;78:131–7.